

**Efficient Interconnecting Layer in Monolithic All-Perovskite
Tandem Solar Cells**

Journal:	<i>Energy & Environmental Science</i>
Manuscript ID	EE-REV-03-2022-000731.R1
Article Type:	Review Article
Date Submitted by the Author:	16-May-2022
Complete List of Authors:	Zhang, Meng; Georgia Institute of Technology, Materials Science and Engineering; Shandong University, Energy and Power Engineering Lin, Zhiqun; Georgia Institute of Technology, Materials Science and Engineering

Cite this: DOI: 10.1039/c1ee00000x

www.rsc.org/ees

REVIEW

Efficient Interconnecting Layer in Monolithic All-Perovskite Tandem Solar Cells

Meng Zhang, and Zhiqun Lin*

Received (in XXX, XXX) Xth XXXXXXXXX 20XX, Accepted Xth XXXXXXXXX 20XX

DOI: 10.1039/c1ee00000x

Tandem solar cells (TSCs) are widely recognized as an effective device architecture to overcome the spectral loss in single-junction solar cells and surpass the Shockley-Queisser (SQ) limit. Organic-inorganic hybrid perovskites are an emerging class of materials for use in TSCs as light absorbers as they carry a stellar set of intriguing attributes including tunable direct bandgap, large absorption coefficients, high ambipolar carrier mobility, small exciton binding energy, and solution processability. In this context, the ability to engineer all-perovskite TSCs (all-PTSCs) promises new opportunities to render low-cost, low-temperature solution-processing of photovoltaics with markedly enhanced device performance. Notably, efficient interconnecting layer (ICL) represents a key component for high-efficiency monolithic tandem devices as it concurrently imparts good electrical, optical, and mechanical interconnections between the subcells. Particularly, an interdiffusion barrier is required to ensure chemical stability of the bottom cell against solvents for solution-processed all-PTSCs. In this review, the triple functions of ICL noted above and the structural requirements for achieving them, as well as the mechanism underpins efficient recombination in ICL, are first discussed. Subsequently, recent advances in efficient ICLs (i.e., tunnel junction-based ICL and recombination layer-based ICL) implemented for monolithic all-PTSCs are critically examined. Finally, the challenges and future opportunities in rationally designing and developing robust ICLs for high-efficiency and stable all-PTSCs are also presented.

1. Introduction

Metal halide perovskites with general formula of ABX_3 ($A^+ = CH_3NH_3^+$ (MA^+), $CH(NH_2)_2^+$ (FA^+), and Cs^+ ; $B^{2+} = Pb^{2+}$, Sn^{2+} , etc.; $X^- = I^-$ and Br^-) (Figure 1a) possess an array of outstanding optoelectronic properties, including large absorption coefficient ($>10^4 \text{ cm}^{-1}$),¹ high ambipolar carrier mobility ($\sim 10 \text{ cm}^2 \text{ V}^{-1} \text{ s}^{-1}$),² long carrier diffusion length ($>1 \mu\text{m}$),³ inherent tolerance to defects,⁴ etc. The past decade has witnessed unprecedented advances in metal halide perovskite solar cells (PSCs) with power conversion efficiency (PCE) leaping from 3.9% to a certified value of 25.7%.⁵ The PCE of single-junction solar cell (SC) is ultimately dictated by the Shockley-Queisser (SQ) limit due virtually to the limited light absorption and inevitable thermalization loss of the light absorber.⁶ Notably, the convenient bandgap tunability and facile processability render perovskites one of the most appealing candidates for tandem solar cells (TSCs), which offer an efficient strategy to overcome the single-junction S-Q limit and further promote the development of perovskite-based photovoltaics.

1.1 The Working Mechanism of TSCs

TSCs are constructed to overcome the S-Q limit by introducing multi-absorbers to broaden light absorption and mitigate hot carrier thermalization loss. Henry pioneered a simple graphical method to clearly show the contributions of the intrinsic losses in ideal SCs, including spectral loss and radiative recombination loss (Figure 1c-d).⁷ The spectral loss contains two parts, that is, energy lower than the bandgap ($h\nu < E_g$) at which photons cannot be utilized (represented by yellow slashes in Figure 1c), and $h\nu > E_g$ where thermalization loss occurs (yellow backslashes; Figure 1c). Despite the spectral loss, the work done by each absorbed photon at the maximum power point (W_{MPP}) is limited by the radiative recombination ($W < E_g$; yellow straight lines, Figure 1c). Therefore, the power per unit area delivered to the load in single-junction SCs is depicted by the light-green area (Figure 1c). It is notable that the S-Q limit of single-junction SCs is 33.7% with a E_g of light absorber of 1.34 eV under 1 sun illumination.⁶ In contrast, two-junction (2J) TSCs enable significantly reduced spectral loss as high-energy photons are absorbed by the top subcell with a larger E_g and low-energy

Broader context

In recent years, the need for renewable and sustainable energy resources has dramatically increased due to the depletion of fossil fuel resources. Photovoltaics carry great potential to solve current energy and environmental issues. Notably, tandem solar cells (TSCs) consisting of multiple light absorbers with considerably different band gaps are promising in breaking the Shockley-Queisser (S-Q) efficiency limit of single junction solar cell via increasing the overall power output of solar modules at low cost. Monolithic TSCs exercise the same working mechanism as single-junction counterparts, yet containing an interconnecting layer (ICL) as an additional key constituent to concurrently provide electric, optical, and mechanical interconnections. In this review, we systematically summarize recent advances in rational design of ICL in all-perovskite TSCs (all-PTSCs), which represents a rapid-evolving cutting-edge research field in TSCs. This timely review will guide future fundamental and applied research on ICL in all-PTSCs and a wide range of other forms of TSCs.

photons are harvested by the bottom subcell with a smaller E_g . On the basis of Henry's graphical efficiency analysis, by varying the E_g of light absorbing materials in 2J TSCs, the theoretical PCE of TSCs is markedly increased as represented by enlarged light-green area with a step (**Figure 1d**). Under 1 sun irradiation, the theoretical PCEs for TSCs with 2J, three junctions (3J), and infinite number of junctions are $\sim 46\%$, $\sim 50\%$, and 65% , respectively. In particular, a PCE of 86.8% is attainable with an infinite number of junctions under highly concentrated sunlight.⁷ Specifically, there are two typical configurations of TSCs, depending on the connection form of subcells, that is, mechanically-integrated four-terminal (4-T) and monolithically-integrated two-terminal (2-T) configurations. 4-T configuration has not found any industrial applications as it involves higher overall cost and greater optical losses compared to its 2-T counterpart. In this context, monolithically-integrated 2-T all-PTSCs stands out as a commercially viable configuration with respect to potentially lighter weight and lower cost for installation.

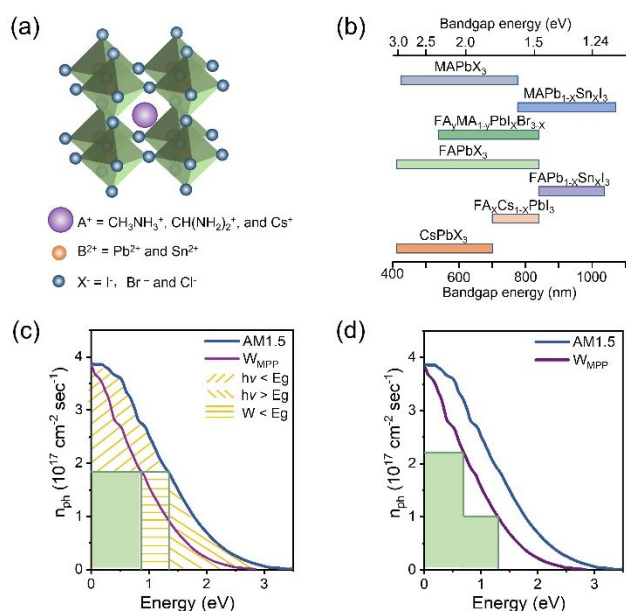


Figure 1. (a) Crystal structure of perovskite ABX₃. (b) Bandgaps of a set of perovskites. Reproduced with permission from Ref. 8. Copyright 2017, Elsevier. (c-d) Graphical analysis of the efficiency of an ideal (c) single-junction solar cell and (d) two-junction tandem solar cell (2J TSC) under standard AM 1.5G spectral irradiance. W_{MPP} represents the work done per absorbed photon at the maximum power point. (c-d) are modified from Ref. 7. Copyright 1980, AIP Publishing.

1.2 The Advantages of All-PTSCs over Other Perovskite-based TSCs

It has been demonstrated that a front subcell with a bandgap of 1.70–1.9 eV and a rear subcell with a bandgap of 0.9–1.2 eV constitute a most optimal 2J TSCs.^{9–11} It is noteworthy that the bandgap of perovskites can also be readily tailored over a large range from 1.17 eV to 3 eV by simply engineering composition of X and B sites (**Figure 1b**). The absorption onset blue-shifts with the substitution of halide of larger radius with

smaller ones (i.e., I⁻ > Br⁻ > Cl⁻). Importantly, the tuning of the I/Br ratio in Pb halide perovskites progressively alters their bandgap from 1.58 eV to 2.28 eV (785 nm to 544 nm), 1.48 eV to 2.23 eV (840 nm to 556 nm), and 1.80 eV to 2.35 eV (690 nm to 528 nm) for A = MA⁺, FA⁺, and Cs⁺, respectively.^{12–14} Incorporation of Cl⁻ further expands the bandgap up to ~ 3 eV.⁸ Substituting Pb with Sn could lower the bandgap (1.3 eV for CsSnI₃, 1.3 eV for MASnI₃, 1.41 eV for FASnI₃).¹⁵ Interestingly, partial incorporation of Sn into Pb-based perovskites greatly lowers the bandgap to 1.17 eV as in MASn_xPb_{1-x}I₃ where 0.8 > x > 0.5.¹⁶ Such bandgap tuning from MAPbI₃ (1.55 eV) to MASnI₃ (1.30 eV) does not follow the Vegard's law with a monotonic bandgap decrease, which is due possibly to the competition between the spin-orbit coupling and lattice distortion.¹⁷ Low Sn-containing MASn_xPb_{1-x}I₃ perovskites (x < 0.5) share tetragonal *I4cm* structure of β -MAPbI₃, while high Sn-containing perovskites (x > 0.5) show the pseudocubic tetragonal *P4mm* structure of α -MASnI₃.¹⁶

As discussed above, the tunable optical absorption of perovskite halides from NIR to visible region positions them well for constructing all-perovskite TSCs (all-PTSCs) and hybrid TSCs with various counterparts, including silicon (Si) solar cells, Cu(In,Ga)Se₂ (CIGS) solar cells, organic solar cells, dye sensitized solar cells, and quantum dot solar cells, etc. Among all perovskite incorporated TSCs, perovskite/Si, perovskite/CIGS, and all-PTSCs are the most promising ones due to their high efficiencies, of which the record efficiencies have reached 29.8%, 24.2%, and 26.4%, respectively.⁵ Perovskite/Si TSCs are expected to realize industry application first due to the dominate position of Si solar cells in the market and their mature scaled production. Perovskite/CIGS TSCs and all-PTSCs represent prospective alternatives to perovskite/Si since the Si subcell can't be processed on flexible substrates and is hard to tune the band gap. Yet, in the long term, the ability of low-temperature solution-processing of all-PTSCs contrasts it sharply to perovskite/Si and perovskite/CIGS TSCs, where the bottom cells (CIGS or Si) of high PCEs are only yielded via vacuum-deposition methods. Solution processing approaches are advantageous in terms of cost-effectiveness and fabrication flexibility, thereby rendering all-PTSCs compatible with flexible substrates via a roll-to-roll manufacturing for future commercialization. It has been estimated that the cost of all-PTSCs is only 1/2–1/3 of that of the perovskite/Si TSCs.¹⁸ Thus, all-PTSCs has been considered as the ultimate goal owing to their high efficiencies, low-cost solution processability, and compatibility with flexible devices, etc.

Benefiting from the progress of mixed Pb–Sn halide perovskites with narrower bandgaps as the rear subcell, the past several years has witnessed rapid advances in high-efficiency monolithic all-PTSCs via rational optimization of perovskite bandgap, device fabrication, and improvement over interconnecting layer (ICL).^{18, 19} Notably, the PCE of 2J (3J) all-PTSCs has boosted from initial 10% (6.7%) to 26.4%²⁰ (20.1%²¹) lately (**Figure 2**). In sharp contrast to copious work on single-junction PSCs, investigation into monolithic all-PTSCs has been comparatively few and limited in scope (**Table 1**). The ability to tailor interconnecting layer (ICL) that renders effective electrical, optical, and mechanical interconnections between the subcells

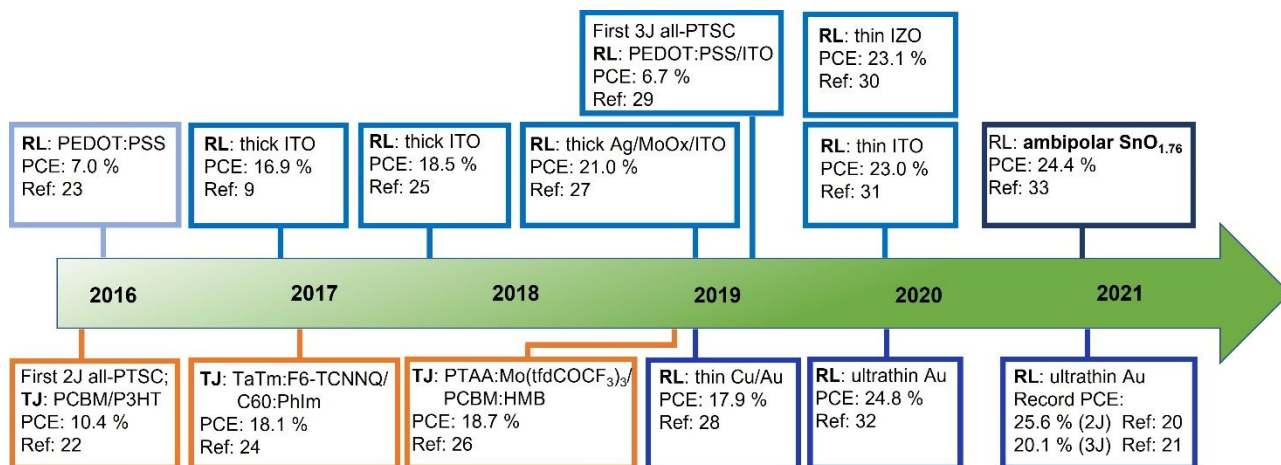


Figure 2. Timeline and the PCE evolution of monolithic all-perovskite tandem solar cells (all-PTSCs) with different interconnecting layers (ICLs; information is exacted from Refs^{10, 20-33}). Orange boxes: all-PTSCs with tunnel junction (TJ)-based ICL. Blue boxes: all-PTSCs with recombination layer (RL)-based ICL, including PEDOT:PSS RL, ITO RL and ultrathin Au RL, ambipolar material-based RL.

represents an important endeavor towards high-efficiency monolithic all-PTSCs. Notably, compared to much research on light absorbers in subcells, rare attention has been concentrated on engineering ICL in TSCs, and not surprisingly, far less in all-PTSCs. In this review, we aim to provide fundamental insight into the ICL in all-PTSCs. First, the key characteristics required for robust ICL (i.e., electrically, optically, and mechanically interconnected) to ensure efficient charge carrier recombination in ICL is discussed. Afterward, recent advances in state-of-the-art ICLs, both tunnel junction-based ICL and recombination layer-based ICL, implemented in all-PTSCs are closely assessed. Finally, the challenges and future directions in crafting practical ICLs for high-performance all-PTSCs are provided.

2. Key Attributes of Robust ICL for All-PTSCs

The introduction of ICL in monolithic TSCs represents an additional key parameter that strongly dictates the overall performance of TSCs as it simultaneously affects short-circuit current density (J_{sc}), fill factor (FF) and open-circuit voltage (V_{oc}) of the tandem devices by imparting good electrical, optical, and mechanical interconnection between the subcells. Particularly, robust mechanical interconnection of ICL is greatly needed in all-PTSCs to ensure chemical stability of the front cell since the precursor solution in fabricating the front and rear subcells share the same type of strong polar solvents (i.e., dimethylformamide (DMF) and dimethylsulfoxide (DMSO)). Actually, there are three strategies to avoid damaging the front subcell when depositing the rear subcell: (1) process the rear subcell using non-solution approach, i.e., evaporation; (2) develop orthogonal solvents for the rear subcell; and (3) deploy a dense ICL as an interdiffusion barrier against solvents. However, it is currently very challenging to fabricate efficient mixed Pb–Sn narrow-bandgap perovskite devices through evaporation approach or with alternative solvents to DMF and DMSO.^{29, 34} In shade of the difficulty with the former two strategies and the advantages of solution processing, a dense ICL as a solvent barrier in all-PTSCs is thus highlighted at this stage.

2.1 Electrical Interconnection

The electrical interconnection of ICL in TSCs has two important aspects, that is, (1) form ohmic contact and extract carriers from adjacent subcells with opposite polarities; and (2) promote the recombination of electrons and holes from these subcells. The working mechanism of each subcell in monolithic all-PTSCs is the same as single-junction PSCs. Electrons and holes are extracted to n-type electron transport layer (ETL) and p-type hole transport layer (HTL) in each subcell, respectively, and further annihilate each other within ICL. Notably, as ETL usually possesses a relatively low work function while HTL demonstrates a relatively high work function for efficient carrier extraction in PSCs, their work function difference builds a significant barrier for current flow. Thus, direct connection of p-type HTL in one subcell with n-type ETL in the other subcell may form a p–n junction with opposite direction to that of the subcells (**Figure 3a**), thereby reducing the open-circuit voltage (V_{oc}) of all-PTSCs.

Generally, there are two effective strategies to eliminate the parasitic diode and enable efficient charge recombination from subcells, that is, introducing a tunneling junction (**Figure 3b**) and inserting a recombination layer (**Figure 3c**). The former comprising degenerately-doped p–n junctions (p^{++} – n^{++}) is ideal for connecting two p–n junctions without experiencing a voltage drop.³⁵ As the width of the depletion region at the semiconductor junction follows:

$$l_{depletion} = \sqrt{\frac{2\epsilon(\Phi_0 - V)N_A + N_D}{q N_A N_D}}$$

where ϵ is the dielectric permittivity of semiconductor; N_A and N_D are the number of ionized acceptors and donors per unit length, respectively; Φ_0 is the built-in voltage, and V is the applied bias. Thus, high doping concentration (p^{++} and n^{++}) significantly reduces the width of depletion region. In practical application, high dopant concentration of approximately $>10^{19}$ cm^{-3} is usually applied.³⁵ With the extremely narrowed depletion

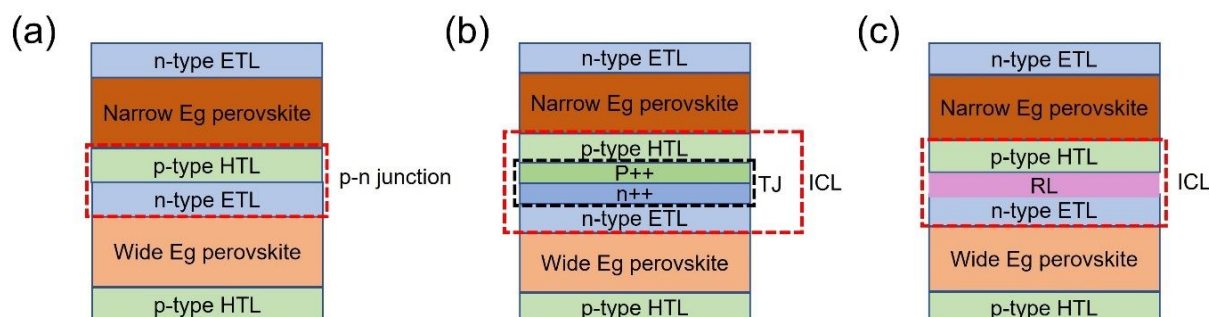


Figure 3. Schematic diagrams of (a) perovskite subcells in all-PTSCs connected without ICL leading to parasitic diode, and (b-c) perovskite subcells in all-PTSCs connected with ICL composed of (b) tunnel junction and (c) recombination layer, where TJ and RL refer to tunneling junction and recombination layer, respectively.

region, carriers can easily tunnel through the depletion region to recombine with counter carriers extracted from neighboring subcell. Meanwhile, Φ_0 must be low enough so energy states of some electrons that tunnel is equal to energy states of holes available on the other side of the barrier. Consequently, current density through the tunnel junction is high while the resistance and Φ_0 are extremely low. ICL based on tunnel junction has been widely applied in III-V semiconductor TSCs, as III-V semiconductors usually satisfy the condition of degenerate doping to achieve atomically sharp homojunctions through epitaxial growth via high-vacuum deposition techniques.³⁶ However, it is usually enormously difficult to attain degenerate doping in both constituents of a heterojunction, especially for the broadly used carrier transport layers in PSCs.

As noted above, the second strategy for removing the parasitic diode is to introduce a recombination layer based ICL, providing the recombination site for carriers extracted from different subcells in all-PTSCs (Figure 3c). Such ICL has been widely employed in many TSCs, such as organic TSCs³⁷ and silicon TSCs,^{9, 38} as it can conveniently adopt the original materials of HTL and ETL and the structures of individual subcells. Regarding the recombination layer, there are three main requirements, that is, (1) appropriate work function to form ohmic contact with the charge extraction layers from different subcells of opposite polarities; (2) high carrier mobility to facilitate charge recombination within the recombination layer; and (3) low lateral conductivity to prevent shunts due to in-plane conduction of the current from the top subcell to large areas of the bottom subcell.

3.2 Optical Interconnection

Based on Kirchhoff's law, the V_{oc} in monolithic TSCs is the sum of the voltages generated from the two subcells, whereas the J_{sc} equals to that of the subcell with the lowest produced current. To maximize the PCE of TSCs, the sub-cells should have equal current densities at their respective maximum power point (MPP), which can be generally achieved by engineering the spectral response or quantum efficiency of the subcells. In this context, ideal ICL positioned between the subcells is required to be highly optically transparent, particularly in the NIR region, to

reduce the optical absorption losses to the narrow-bandgap subcell. Currently, ICL in all-PTSCs is usually structured as HTL/recombination layer/ETL (Figure 4 and Table 1), thus light management in ICL should be conducted from two sides, i.e., both charge transport layers and recombination layer. Comprehensive consideration on the polarity and materials selection of tandem cells is imperative for better compatibility of materials and fabrication process. For example, the most commonly used hole transport material, spiro-OMeTAD, has been identified as a disqualified HTL candidate for p-i-n structured single junction SCs due to strong parasitic absorption losses in the blue and UV spectral region. Yet, this does not affect its application in ICL for all-PTSCs since the absorption of spiro-OMeTAD is not to be compared with that of wide bandgap perovskite.

3.3 Mechanical Interconnection

The requirement to ICL for mechanical connection between subcells can be discussed from the viewpoint of device fabrication. During fabrication, firstly, the processing condition of ICL should not damage the underneath subcell, as the perovskite absorber can be easily destroyed by high-energy or high-temperature process.³⁹ Secondly, ICL itself should be stable enough against the fabrication of the top subcell. Lastly, ICL needs to provide a good interdiffusion barrier to solvent penetration for solution-processed all-PTSCs in order to protect the underlying subcells. After fabrication, the effectiveness of mechanical interconnection of ICL is largely reflected by its long-term stability in (1) avoiding ions penetration from subcells into each other, and (2) preventing the detachment of itself or other layers above it.

3. State-of-the-Art ICLs in all-PTSCs

Figure 4 summarizes the V_{oc} loss, PCE and FF in state-of-the-art ICLs used in 2J all-PTSCs. As noted in Section 2.1, tunnel junction (TJ)-based ICL and recombination layer (RL)-based ICL represent two effective ICLs that render efficient charge recombination from subcells. Notably, investigation into TJ-based ICL for all-PTSCs is comparatively few and limited in scope, as discussed in Section 3.1. To date, four RL-based ICLs (i.e., transparent conducting oxides (TCO) RL, ultrathin metal RL,

Cite this: DOI: 10.1039/c1ee00000x

www.rsc.org/ees

REVIEW

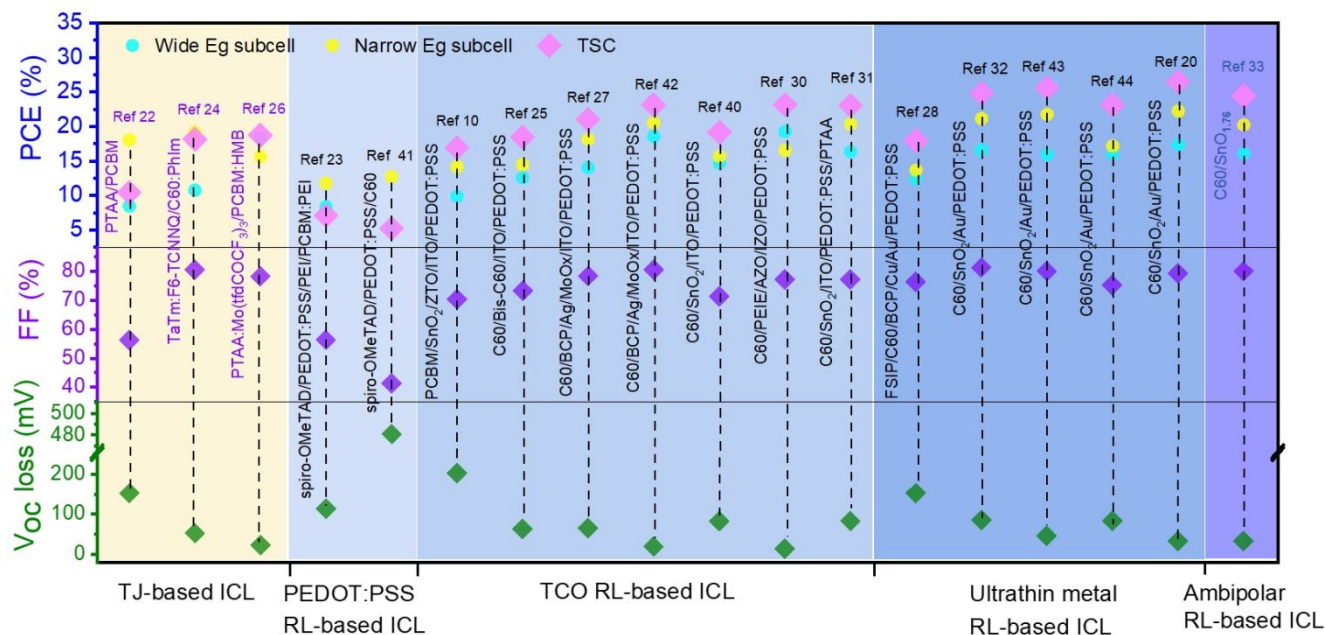


Figure 4. PCE, FF and Voc loss of monolithic 2-junction all-perovskite tandem solar cells (all-PTSCs) with different interconnecting layer (ICL). Information extracted from Refs 10, 20, 22–28, 30–33, 40–44. The ICL induced Voc loss in TSC is calculated by: $V_{oc\ loss} = V_{oc1}(\text{Wide Eg subcell}) + V_{oc2}(\text{Narrow Eg subcell}) - V_{oc}(\text{TSC})$.

highly conductive poly(3,4-ethylenedioxythiophene)-poly(styrenesulfonate) (PEDOT:PSS) RL, and ambipolar $\text{SnO}_{1.76}$ RL have been reported. In what follows, recent advances in these state-of-the-art ICLs are scrutinized.

3.1 Tunnel Junction (TJ)-based ICL

Most of ETL and HTL materials employed in single junction PSCs have low lateral conductivity and high charge selectivity. Yet, the simple ETL/HTL stack interface cannot ensure a fast recombination of carriers from the individual subcell, thereby disqualifying it as an efficient recombination junction for monolithic all-PTSCs. Notably, large Voc loss was seen using such rough ETL/HTL interface-based ICL, leading to low FF and PCE in all-PTSCs.²² More efficient tunnel junction based on ETL/HTL stack can be constructed through further doping of ETL and HTL, resulting in significantly decreased Voc loss and greatly improved FF in the corresponding all-PTSCs (Figure 4).^{24, 26} There are two key issues associated with the implementation of TJ-based ICL in all-PTSCs: (a) it is difficult to concurrently attain degenerate doping in both ETL and HTL materials, and (2) the ETL/HTL, often solution-processed, is not dense enough to function as a chemical barrier during the solution processing of the top subcell.^{22, 24, 26} It is notable that recent studies on TJ-based ICL in all-PTSCs are not conducted using perovskites with optimized bandgap and film thickness of the subcells, leading to

small Jsc and low PCE of TSCs (Table 1). Thus, it is challenging to accurately evaluate the performance of these TJ-based ICLs in the corresponding devices. As such, investigation into TJ-based ICLs with optimized subcells is highly desirable to render their further improvement.

The first implementation of ICL in 2J monolithic all-PTSCs was reported in 2016 by simply stacking the poly(3-hexylthiophene-2,5-diyl) (P3HT) or Poly[bis(4-phenyl)(2,5,6-trimethylphenyl)amine] (PTAA) HTL of one subcell with PCBM of the other subcell (Figure 5a).²² The two subcells are laminated by pressurizing with a clip and subsequently dried to yield TSCs. However, a thick HTL (~2000 nm) is needed to maintain the adhesion between the two subcells during the lamination process, which imposes a significant barrier for carrier recombination due to the low conductivity of thick HTL. By introducing Bis(trifluoromethylsulfonyl)amine lithium salt (Li-TFSI) and 4-tert-butylpyridine (t-BP) additives in P3HT or PTAA HTL, their conductivity displays a significant 40-fold increase due to the Li/Li⁺ redox shuttling,⁴⁵ thus facilitating hole transport and carrier recombination at the P3HT/PCBM or PTAA/PCBM interface.²² Further doping of ETL and HTL is developed to construct more efficient tunnel junction with decreased depletion width as ICL (Figure 5b).²⁴ Specifically, to avoid solvent damage during the spin-coating process, both ICL and the rear subcell are fabricated through thermal evaporation. The

structure of the ICL is $N4,N4,N4'',N4''$ -tetra([1,1'-biphenyl]4-yl)-[1,1':4',1''-terphenyl]-4,4''-diamine (TaTm)/ TaTm:2,2'-(perfluoronaphthalene-2,6-diylidene) (F_6 -TCNNQ)/ C_{60} : $N1,N4$ -bis(tri-*p*-tolylphosphoranylidene) benzene-1,4-diamine (PhIm)/ C_{60} , in which F_6 -TCNNQ and PhIm are used as the dopants in TaTm HTL and C_{60} ETL, respectively.²⁴ Notably, the conductivity of TaTm can be largely increased by two orders of magnitude through F_6 -TCNNQ doping.⁴⁶ Electrons and holes are efficiently recombined in the tunnel junction of TaTm: F_6 -TCNNQ/ C_{60} :PhIm with only 49 mV of V_{oc} loss in the champion device. Despite the absence of optimized bandgaps, the $CS_{0.15}FA_{0.85}Pb(I_{0.3}Br_{0.7})_3$ -MAPbI₃ TSC demonstrates a record PCE of 18.1% with a V_{oc} of 2.29 V.²⁴ The tunnel junction with the identical structure has also been exercised in a MAPbI₃-MAPbI₃ TSC.⁴⁷

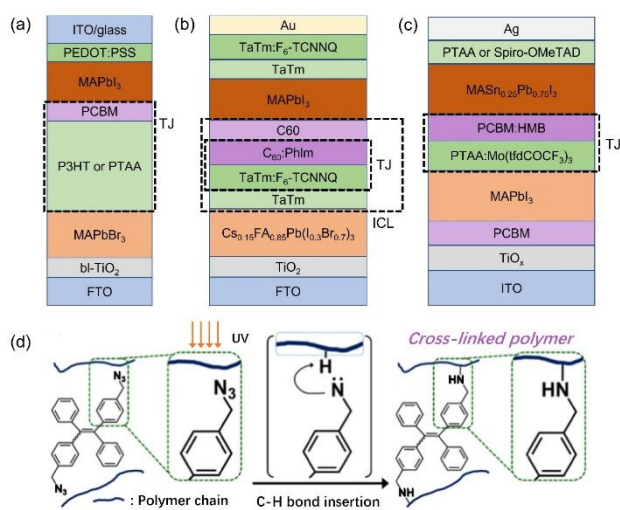


Figure 5. Schematic illustration of all-PTSC architectures with a tunnel junction-based ICL composed of (a) P3HT/PCBM or PTAA/PCBM; (Modified from Ref ²². Copyright 2015, John Wiley and Sons.) (b) TaTm: F_6 -TCNNQ/ C_{60} :PhIm; (Modified from Ref ²⁴. Copyright 2016, John Wiley and Sons.) (c) PTAA: Mo(tfdCOCF₃)₃/PCBM:HMB. (Modified from Ref ²⁶. Copyright 2019, Elsevier.) (d) Schematic of crosslinking of PTAA by TPE-MN3 via C-H insertion of nitrene radicals generated by UV irradiation. Reproduced with permission from Ref ²⁶, Copyright 2019, Elsevier.

In order to render solution processing of the entire all-PTSCs, an ICL comprising crosslinked p-doped HTL (PTAA) and n-doped fullerene ETL (PCBM) was developed (Figure 5c).²⁶ PTAA is crosslinked with 1,2-bis[4-(azidomethyl) phenyl]-1,2-diphenylethane (TPE-MN3; crosslinker) under UV-irradiation (Figure 5d), resulting in dense and robust polymer network with high solvent resistance. The incorporation of p-type dopant molybdenum tris-[1-(trifluoroethanoyl)-2-(trifluoromethyl)ethane-1,2-dithiolene] [Mo(tfdCOCF₃)₃] in PTAA dramatically increases the thick film conductivity by more than three orders of magnitude. On the other hand, hexamethonium bromide (HMB) is adopted to dope PCBM. The crosslinked PTAA: Mo(tfdCOCF₃)₃/PCBM:HMB tunnel junction affords a PCE up to 18.69% in solution-processed all-PTSCs.²⁶ Recently, covalent

crosslinkable materials have been successfully exploited as HTL⁴⁸ or ETL⁴⁹ in single-junction PSCs to improve their efficiency and ambient and thermal stability. The introduction of crosslinked carrier transport layers in ICL offers a promising strategy to enhance solvent resistance and ensure the structural integrity of ICL upon depositing the subsequent layers.

3.2 Recombination Layer (RL)-based ICL

As noted above, TCO, ultrathin metal, highly conductive PEDOT:PSS, and ambipolar SnO_{1.76} have been exercised as recombination layer (RL) in ICL for all-PTSCs. Highly conductive PEDOT:PSS RL-based ICL is an early attempt and has only been implemented for n-i-p-structured all-PTSCs (Figure 4 and Table 1). In comparison, p-i-n-structured all-PTSCs with either a TCO RL or an ultrathin metal RL are more widely investigated. Though relatively small V_{oc} loss and high FF are achieved with both TCO and ultrathin metal RLs (Figure 4), significant concerns rise from TCO RL due to the need of high-energy deposition process and its high lateral conductivity. As such, ultrathin metal RL stands out as a more promising RL employed in all-PTSCs. Specifically, the recent developed ambipolar material-based RL greatly simplifies the conventional RL-based ICL, thereby affording a unique platform for rational design and implementation of novel, simplified ICLs for TSCs.

3.2.1 TCO RL

Transparent conducting oxides (TCOs), such as indium tin oxide (ITO), indium-doped zinc oxide (IZO), and fluorine-doped SnO₂ (FTO), possess both high electrical conductivity and optical transmittance in the visible and near-infrared (NIR) regions, making them perfect candidates as RL to construct ICL by pairing with appropriate ETL and HTL in all-PTSCs. TCOs are usually deposited by magnetron sputtering at high temperature to enable high electrical and optical properties; this technique, however, represents a double-edged sword to its application in ICL. Clearly, the dense and compact nature of sputtered TCOs could perform as an effective physical barrier and render chemical stability of the bottom cell against solvents during the fabrication of the top cell. However, the high kinetic energy of sputtered particles may damage the underlying soft layers. In order to protect the perovskite and organic carrier-extraction layers from damage during sputtering, a buffer layer prepared at low temperature is required. In principle, the buffer layer should be highly optically transparent with a large bandgap, energetically well-aligned for carrier-selective contact, and chemically stable with the contacts (i.e., TCO and carrier transport layer).³⁸ Additionally, the buffer layer may function as a diffusion barrier to prevent both organic cation evolution and moisture penetration, thereby overcoming the thermal and environmental instability of PSCs.⁵⁰ Metal oxides prepared via atomic layer deposition (ALD) and thermal evaporation, such as SnO₂,¹⁰ MoOx,²⁷ AZO,³⁰ are thus judiciously chosen. Notably, significant performance improvements, especially FF (often > 0.75), are achieved in all-PTSCs with TCO RL due largely to reduced resistive losses enabled by the high conductivity of TCOs.

The first report on the ITO RL-based ICL involves a complex structure of PCBM/SnO₂/ZTO/ITO/PEDOT:PSS (Figure 6a).¹⁰ The

Cite this: DOI: 10.1039/c1ee00000x

www.rsc.org/ees

REVIEW

Table 1. Summary of the structures, fabrication and thickness of ICL in all-PTSCs. Note: The two ICLs in 3J all-PTSCs share the same or similar structures, thus only the ICL between front cell and central cell is listed in **Table 1**; evaporation refers to thermal evaporation.

Junction	Polarity	Front Subcell	ICL			Rear Subcell	Voc (V)	Jsc (mA/cm ²)	FF (%)	PCE (%)	Year	Ref.
			HTL (ETL)	Recombination layer	ETL (HTL)							
2J	n-i-p	MAPbBr ₃ Spin-coating	PTAA Drop-casting (2000 nm)	/	PCBM Spin-coating (50 nm)	MAPbI ₃ Spin-coating	2.25	8.30	56	10.40	2015	22
2J	n-i-p	MAPbI ₃ Spin-coating	spiro-OMeTAD Spin-coating (150 nm)	PEDOT:PSS/PEI Film lamination (40 nm/3 nm) transfer	PCBM:PEI Spin-coating (40 nm)	MAPbI ₃ Spin-coating	1.89	6.61	56	7.00	2015	23
2J	p-i-n	FA _{0.83} CS _{0.17} Pb(I _{0.5} Br _{0.5}) ₃ Spin-coating	PCBM/SnO ₂ /ZTO Evaporation/ALD (10 nm/4 nm/2 nm)	ITO Sputtering (100 nm)	PEDOT:PSS Spin-coating	FA _{0.75} CS _{0.25} Sn _{0.5} Pb _{0.5} I ₃ Spin-coating	1.66	14.50	70	16.90	2016	10
2J	n-i-p	CS _{0.15} FA _{0.85} Pb(I _{0.3} Br _{0.7}) ₃ Spin-coating	TaTm/TaTm:F6-TCNNQ Evaporation (10 nm/40 nm)	/	C60:PhIm/C60 Evaporation (40 nm)	MAPbI ₃ Evaporation	2.29	9.83	80	18.10	2017	24
2J	p-i-n	MA _{0.9} CS _{0.1} Pb(I _{0.6} Br _{0.4}) ₃ Spin-coating	C60/Bis-C60 Evaporation/spin-coating (50 nm/10nm)	ITO Sputtering (100 nm)	PEDOT:PSS Spin-coating (30 nm)	MAPb _{0.5} Sn _{0.5} I ₃ Spin-coating	1.98	12.70	73	18.50	2017	25
2J	n-i-p	MAPbBr ₃ Spin-coating & vapor interdiffusion	spiro-OMeTAD Spin-coating (185 nm)	PEDOT:PSS Spin-coating (80 nm)	C60 Spin-coating (30 nm)	MAPbI ₃ Spin-coating & vapor interdiffusion	1.96	6.40	41	5.10	2017	41
2J	p-i-n	FA _{0.83} CS _{0.17} Pb(I _{0.5} Br _{0.5}) ₃ Spin-coating	FSIP/C60/BCP Spin-coating/evaporation (5 nm/40 nm/8 nm)	Cu/Au Evaporation (0.6 nm/6 nm)	PEDOT:PSS Spin-coating (20 nm)	FA _{0.5} MA _{0.5} Pb _{0.5} Sn _{0.5} I ₃ Spin-coating	1.86	12.61	76	17.90	2018	28
2J	p-i-n	FA _{0.8} CS _{0.2} Pb(I _{0.7} Br _{0.3}) ₃ Spin-coating	C60/BCP Evaporation	Ag/MoOx/ITO Evaporation/sputtering	PEDOT:PSS Spin-coating	(FASnI ₃) _{0.6} (MAPbI ₃) _{0.4} Spin-coating	1.922	14.00	78	21.00	2018	27

			(20 nm/5 nm)	(1 nm/3 nm/120 nm)	(20 nm)							
2J	p-i-n	$\text{FA}_{0.6}\text{Cs}_{0.4}\text{Pb}(\text{I}_{0.7}\text{Br}_{0.3})_3$	C60/SnO ₂	ITO	PEDOT:PSS	$\text{FA}_{0.75}\text{Cs}_{0.25}\text{Sn}_{0.5}\text{Pb}_{0.5}\text{I}_3$	1.81	14.80	71	19.10	2018	⁴⁰
		Spin-coating	Evaporation/ALD (40 nm/10 nm)	Sputtering (120 nm)	Spin-coating (30 nm)	Spin-coating						
2J	p-i-n	$\text{FA}_{0.6}\text{Cs}_{0.3}\text{DMA}_{0.1}\text{PbI}_{2.4}\text{Br}_{0.6}$	C60/PEIE	AZO/IZO	PEDOT:PSS	$\text{FA}_{0.75}\text{Cs}_{0.25}\text{Sn}_{0.5}\text{Pb}_{0.5}\text{I}_3$	1.88	16.00	77	23.10	2019	³⁰
		Spin-coating	Evaporation/spin-coating (30 nm/1 nm)	ALD/sputtering (25 nm/5 nm)	Spin-coating (20 nm)	Spin-coating						
2J	p-i-n	$\text{Cs}_{0.2}\text{FA}_{0.8}\text{PbI}_{1.8}\text{Br}_{1.2}$	C60/SnO ₂	Au	PEDOT:PSS	$\text{MA}_{0.3}\text{FA}_{0.7}\text{Pb}_{0.5}\text{Sn}_{0.5}\text{I}_3$	1.96	15.60	81	24.80	2019	³²
		Spin-coating	Evaporation/ALD (20 nm/20 nm)	evaporation (1 nm)	Spin-coating	Spin-coating						
2J	p-i-n	$\text{FA}_{0.6}\text{Cs}_{0.4}\text{Pb}(\text{I}_{0.65}\text{Br}_{0.35})_3$	C60/SnO ₂	ITO	PEDOT:PSS/PTAA	$\text{FA}_{0.5}\text{MA}_{0.45}\text{Cs}_{0.05}\text{Pb}_{0.5}\text{Sn}_{0.5}\text{I}_3$	1.99	15.10	77	23.00	2019	³¹
		Spin-coating	Evaporation/ALD (30 nm/13 nm)	sputtering (10 nm)	Spin-coating	Spin-coating						
2J	n-i-p	MAPbI ₃	cross-linked PTAA:Mo(tfdCOCF ₃) ₃	/	PCBM:HMB	$\text{MASn}_{0.25}\text{Pb}_{0.75}\text{I}_3$	1.79	13.36	78	18.69	2019	²⁶
		Spin-coating	Spin-coating (90 nm)		Spin-coating (40 nm)	Spin-coating						
2J	p-i-n	$\text{Cs}_{0.2}\text{FA}_{0.8}\text{PbI}_{1.8}\text{Br}_{1.2}$	C60/SnO ₂	Au	PEDOT:PSS	$\text{FA}_{0.7}\text{MA}_{0.3}\text{Pb}_{0.5}\text{Sn}_{0.5}\text{I}_3$	2.01	16.00	80	25.60	2020	⁴³
		Spin-coating	Evaporation/ALD (20 nm/20 nm)	evaporation (1 nm)	Spin-coating	Spin-coating						
2J	p-i-n	$\text{Cs}_{0.4}\text{FA}_{0.6}\text{PbI}_{1.95}\text{Br}_{1.05}$	C60	SnO _{1.76}	/	$\text{Cs}_{0.05}\text{MA}_{0.45}\text{FA}_{0.5}\text{Pb}_{0.5}\text{Sn}_{0.5}\text{I}_3$	2.03	15.20	80	24.40	2020	³³
		Spin-coating	Evaporation (15 nm)	ALD (9 nm)		Spin-coating						
2J	p-i-n	$\text{K}_{0.05}\text{Cs}_{0.05}(\text{FA}_{0.6}\text{MA}_{0.4})_{0.9}$ $\text{Pb}(\text{I}_{0.6}\text{Br}_{0.4})_3$	C60/SnOx	Au	PEDOT:PSS	$\text{FA}_{0.66}\text{MA}_{0.34}\text{Pb}_{0.5}\text{Sn}_{0.5}\text{I}_3$	1.95	15.80	0.75	23.10	2021	⁴⁴
		Spin-coating	Evaporation/ALD (20 nm/45 nm)	Evaporation (1 nm)	Spin-coating (20 nm)	Spin-coating						
2J	p-i-n	$\text{FA}_{0.8}\text{Cs}_{0.2}\text{Pb}(\text{I}_{0.62}\text{Br}_{0.38})_3$	C60/SnO ₂	Au	PEDOT:PSS	$\text{FA}_{0.7}\text{MA}_{0.3}\text{Pb}_{0.5}\text{Sn}_{0.5}\text{I}_3$	2.03	16.5	0.79	26.40	2022	²⁰
		Spin-coating	Evaporation/ALD (20 nm/20 nm)	Evaporation (1 nm)	Spin-coating	Spin-coating						
3J	n-i-p	$\text{FA}_{0.83}\text{Cs}_{0.17}\text{Pb}(\text{Br}_{0.7}\text{I}_{0.3})_3$	spiro-OMeTAD	PEDOT:PSS/ITO	PCBM	Central cell: MAPbI ₃	2.70	8.30	43	6.70	2019	²⁹

		Spin-coating	Spin-coating (50 nm)	Spin-coating (15 nm/50 nm)	Spin-coating (50 nm)	Spin-coating	Rear cell: MAPb _{0.75} Sn _{0.25} I ₃					
3J	p-i-n	Cs _{0.2} FA _{0.8} PbI _{0.9} Br _{2.1}	C60/SnO ₂	Au	NiO/PTAA	Central cell: Cs _{0.05} FA _{0.95} PbI _{2.55} Br _{0.45}	2.80	8.80	81	20.10	2020	21
		Spin-coating	Evaporation/ALD (20 nm/30 nm)	evaporation (1 nm)	Spin-coating (80 nm/8 nm)	Spin-coating						
3J	p-i-n	Cs _{0.1} (FA _{0.66} MA _{0.34}) _{0.9} PbI ₂ Br	C60/SnO ₂	Au	PEDOT:PSS	Central cell: FA _{0.66} MA _{0.34} PbI _{2.85} Br _{0.15}	2.79	7.34	82	16.80	2020	51
		Spin-coating	Evaporation/ALD (20 nm/45 nm)	evaporation (1 nm)	Spin-coating (50 nm)	Spin-coating						

Cite this: DOI: 10.1039/c1ee00000x

www.rsc.org/ees

REVIEW

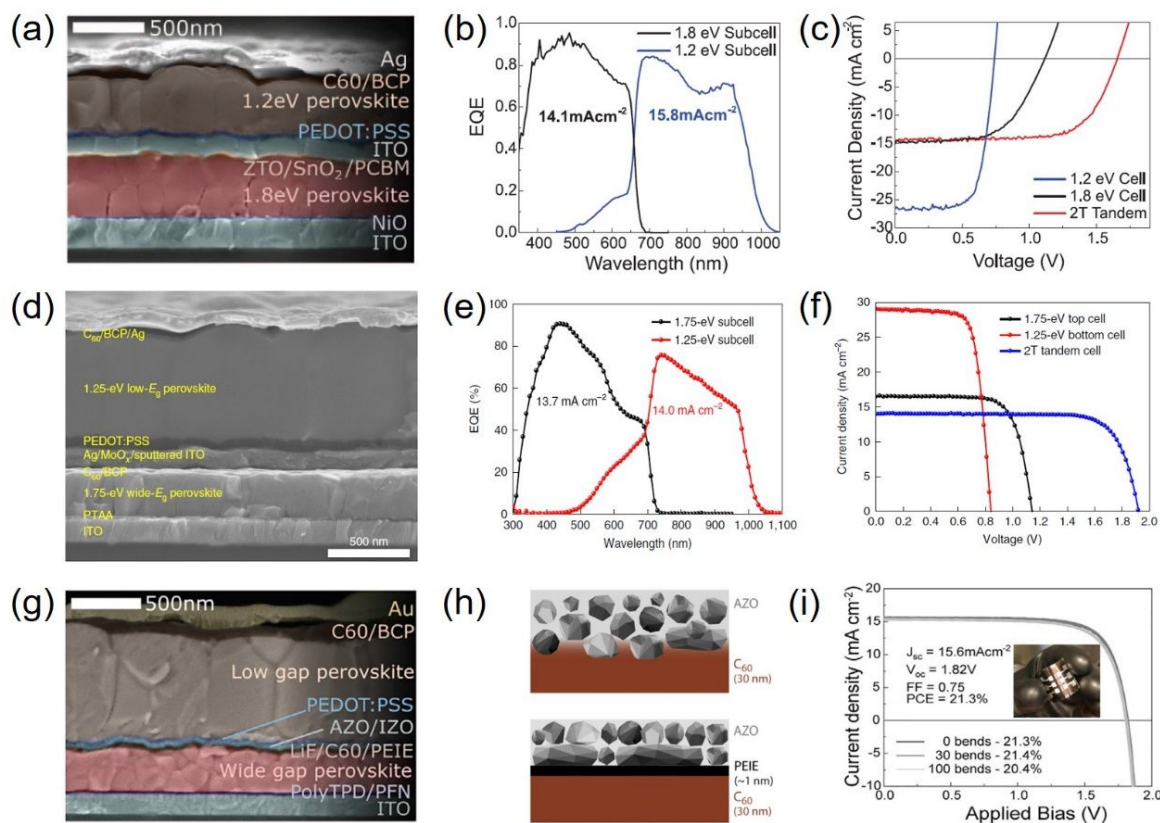


Figure 6. (a) SEM image of all-PTSCs with PCBM/SnO₂/ZTO/ITO/PEDOT:PSS ICL, and the corresponding (b) IPCE spectra and (c) *J-V* curves. (a-c) are reproduced with permission from Ref ¹⁰. Copyright 2016, The American Association for the Advancement of Science. (d) SEM image of all-PTSCs with C₆₀/BCP/Ag/MoO_x/ITO/PEDOT:PSS ICL, and the corresponding (e) IPCE spectra and (f) *J-V* curves. (d-e) are reproduced with permission from Ref ²⁷. Copyright 2018, Springer Nature. (g) SEM image of all-PTSCs with LiF/C₆₀/PEIE/AZO/ITO/PEDOT:PSS ICL, (h) schematic depicting AZO growth on C₆₀ and PEIE-treated C₆₀ surfaces, and (i) the corresponding *J-V* curves of flexible all-PTSCs fabricated on polyethylene naphthalate (PEN). (g-i) are reproduced with permission from Ref ³⁰. Copyright 2019, Elsevier.

thin stack of ALD SnO₂ (4 nm)/ZTO (2nm) layer is used as a buffer
 5 to minimize damage from ITO sputtering. 100-nm thick ITO is
 sputtered to simultaneously serve as a RL and a physical barrier
 against solvents. It is important to note that this is also the first
 all-PTSCs with optimized bandgaps yet non-optimized film
 thickness of perovskite, thus displaying a current density
 10 mismatch of 1.7 mA/cm² from the subcells (**Figure 6b**). However,
 the energetics of ITO relative to adjoining interlayers along with
 its superior electrical conductivity impart effective transfer of
 charge carriers and efficient recombination to reduce electrical
 losses, yielding small *V_{oc}* loss of 200 mV and high FF of 0.7. As a
 15 result, the corresponding 2J all-PTSCs demonstrated a PCE of
 16.9 % for 0.2 cm² device (**Figure 6c**) and 13.8% for 1 cm²

device.¹⁰ Following this pioneering work, ITO has been exploited
 frequently as an efficient RJ in all-PTSCs with continuous
 improvement on ICL.^{25, 27, 31, 40} For example, recently, ITO was
 20 sputtered on the evaporated C₆₀ ETL with only a solution spin-
 coated Bis-C₆₀ buffer layer.²⁵ In another study, thermally
 evaporated molybdenum oxide (MoO_x) (3 nm) was employed as
 the buffer layer for the high-energy ITO sputtering process,
 resulting in a new ICL structure of
 25 C₆₀/BCP/Ag/MoO_x/ITO/PEDOT:PSS (**Figure 6d**).²⁷ The ultrathin
 Ag layer (1 nm) is inserted because of relatively low electrical
 conductivity of MoO_x. Notably, with both optimized perovskite
 bandgaps and film thicknesses, the current density mismatch is
 largely decreased to 0.3 mA/cm² (**Figure 6e**) and a PCE of 21% in

2J all-PTSCs was demonstrated (Figure 6f).²⁷ It is worth noting that the PCE of 2J all-PTSCs has recently been enhanced to 23.1% with negligible V_{oc} loss by adopting the same ICL.⁴² Yet, concerns over long-term stability may raise by using MoO_x as a sputter buffer layer, as iodide in perovskite can chemically react with MoO_x.⁵²

As noted above, the sputtered ITO usually has a thickness of 100-120 nm to block solvent penetration.^{10, 25, 27, 40} However, further development of such a thick ITO RL is greatly challenged by the following three aspects. First, thick ITO induces a more severe parasitic absorption in the near-infrared spectral range, which would decrease J_{sc} and PCE of TSCs. The ITO RL with a thickness of 120 nm only exhibits a transmittance of ~70% over the range of 720-900 nm,²⁷ which restricts light harvesting by the low-bandgap perovskite bottom subcell. Second, thick ITO layer results in shunting between subcells that severely constrains the performance of large-area devices and prevents the cell-to-cell monolithic integration in thin-film modules.⁵³ Finally, the thick ITO is not suitable for applications in flexible devices owing to its brittle nature. In this context, chemical protection has been slowly diverted from ITO RL to the buffer layer during device fabrication (Figure 7).

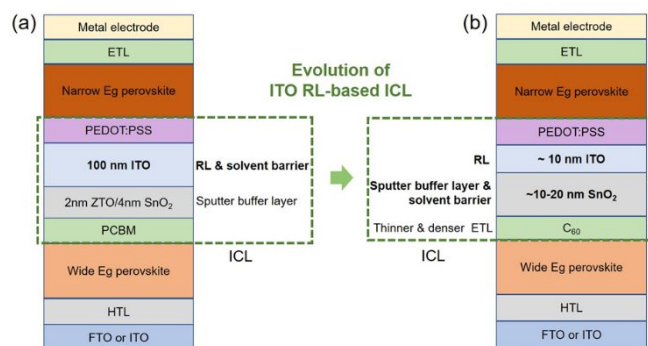


Figure 7. Schematic illustration of all-PTSC architectures with (a) thick ITO (Modified from Ref ¹⁰. Copyright 2016, The American Association for the Advancement of Science.) and (b) thin ITO RL (Modified from Ref ³¹. Copyright 2019, Springer Nature.), where the evolution of efficient ITO RL-based ICL is clearly evident.

Recently, a conformal ALD-aluminum zinc oxide (AZO) layer was developed to concurrently function as a sputter buffer layer and an interdiffusion barrier by using an ultrathin poly(ethylenimine) ethoxylated (PEIE) (1 nm) as nucleation layer (Figure 6g-h).³⁰ The nucleophilic hydroxyl and amine functional groups in PEIE can serve as nucleation sites during the ALD process, resulting in densely-nucleated AZO layer that exhibits substantially improved barrier properties against DMF and H₂O permeation. With this effective solvent barrier, the thickness of the sputtered IZO RL is decreased to as thin as 5 nm while retaining significant carrier combination capability. This thin ICL enables the construction of both rigid and flexible 2J all-PTSCs with high performance of 23.1% and 21.3% (Figure 6i),

respectively.³⁰ Further improvements can be achieved by precisely tuning the growth conditions to yield compact ALD layers without the assistance of a nucleation layer. To this end, recently, a conformal ALD-SnO₂ buffer layer with a thickness of only 12 nm was fabricated which alone prevents solvent damage, while the thicknesses of ITO RL was reduced to 10 nm (Figure 7b).³¹ Notably, an ALD-SnO₂ buffer layer of 10-20 nm is widely implemented in literature.

As high-power deposition of ITO via sputtering stands out as an obstacle that limit the further improvement of ITO RL-based ICL in all-PTSCs, a solution-processed PEDOT:PSS/ITO nanoparticle layer as the RJ is thus developed.²⁹ By employing a highly volatile acetonitrile(CH₃CN)/methylamine(CH₃NH₂) (ACN/MA) solvent-based perovskite solution, the first fully solution-processed monolithic 3J all-PTSC was demonstrated with this PEDOT:PSS/ITO nanoparticle RL. A V_{oc} of 2.83 V is achieved with a three perovskite absorbers of cascade bandgaps of 1.94, 1.57, and 1.24 eV.²⁹ Despite a PCE of only 6.7% from this 3J all-PTSC, this proof of concept opens up new opportunities for large-scale, low-cost, printable perovskite multi-junction solar cells.²⁹ Very recently, a highly efficient interconnect based on an ultrathin ALD-grown InO_x layer with a thickness of only about 1.5 nm was developed for perovskite-organic tandem cells.⁵⁴ As such, low temperature ALD technique shed light on the improved deposition of TCO-based RL for future use in all-PTSCs.

3.2.2 Ultrathin Metal RL

In addition to TCO, ultrathin metal is another extensively used RL. Carrier recombination in ICL is energetically similar to Shockley–Read–Hall (SRH) trap-assisted recombination, yet all carriers involved are majority carriers collected from the respective subcells (rather than one minority and one majority carrier as in the classic SRH case).⁵⁵ Thus, the mechanism of RL-based ICL can be taken as trap-assisted tunneling. Incorporation of metal represents a typical strategy to enhance this mechanism. As an ALD-grown SnO₂ film with exceptional conformality as thin as ~10-20 nm can serve as an excellent chemical barrier to the underneath perovskite and functional layers,³¹ ultrathin metal is thus inserted as RL to replace the sputtered ITO, thereby avoiding the potential damage associated with high-temperature sputtering. In contrast, metal is usually compatible with thermal evaporation which operates at a much lower temperature. Currently, gold (Au) is the most widely used ultrathin metal RL due to its appropriate work function, good conductivity, and stability. Regarding optical transmittance, a thinner metal film is better. In practical application, Au film with a thickness of ~1 nm is adopted for efficient carrier combination while maintaining a large sheet resistance (i.e., low lateral conductivity to reduce shunting).^{20, 21, 32, 43, 44, 51} In the ALD-SnO₂/Au combination, SnO₂ can provide superior carrier extraction as an ETL and act as a solvent barrier. Yet, an additional organic ETL (e.g., C₆₀) is still needed on the bottom perovskite film for protection. This is because ALD technique cannot be applied directly on bare perovskite films as H₂O is used to hydrolyze SnO₂ precursors in the ALD process.

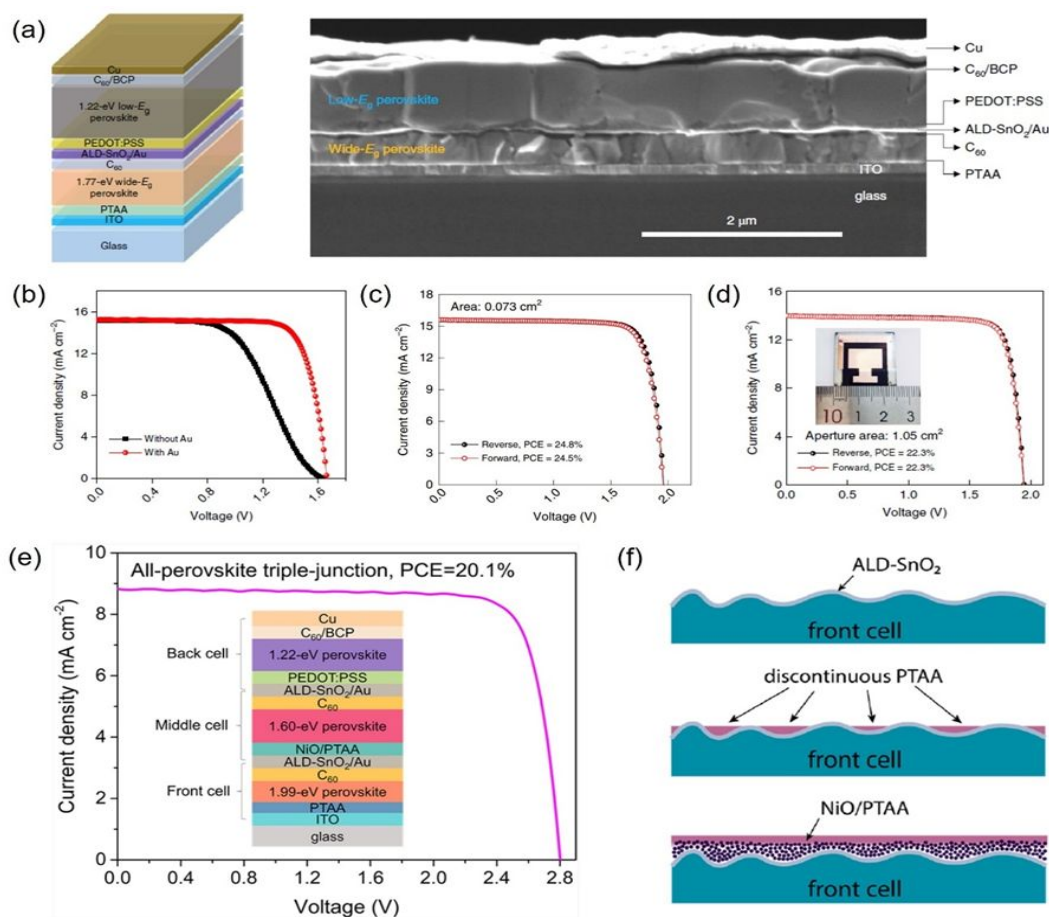


Figure 8. (a) Device structure and the corresponding cross-sectional SEM image of all PTSCs with an ALD-SnO₂/Au-based ICL; (b) *J*–*V* curves of TSCs without and with ultrathin Au layer in ICL; (c–d) *J*–*V* curves of (c) small-area (0.073 cm²) and (d) large-area (1.05 cm²) TSCs. (a–d) are reproduced with permission from Ref.³². Copyright 2019, Springer Nature. (e) Device structure and *J*–*V* curve of 3J all PTSCs with an ALD-SnO₂/Au-based ICL, showing a record PCE of 20.1%. (f) Schematic diagram of PTAA and NiO/PTAA HTL for interface improvement in ICL. (e–f) are reproduced with permission from Ref.²¹. Copyright 2020, American Chemical Society.

The first study of employing ultrathin metal as RL in 2J all-PTSCs has an ICL structure of fluoride silane incorporated PEIE (FSIP) system/C₆₀/BCP/Cu:Au alloy/PEDOT:PSS.²⁸ The FSIP hybrid system is designed to afford chemical protection for the underlying perovskite film. However, large *V*_{oc} loss of 150 mV was found in this work due to energy band mismatch and high optical loss. Robust ALD-SnO₂ is then incorporated as solvent barrier to protect the underneath perovskite and work together with ultrathin metal RL (**Figure 8a**).³² The SnO₂ barrier layer also improved the performance of the wide-bandgap front cells by providing excellent electron extraction.³² Notably, the ultra-thin Au layer (~1 nm) affords efficient electron-hole recombination as the TSCs without the Au layer exhibit an obvious S shape in the *J*–*V* curves near the open-circuit voltage and thus low FF (**Figure 8b**).³² Certified PCEs of 24.8% for small-area devices (0.073 cm², **Figure 8c**) and of 22.1% for large-area devices (1.05 cm², **Figure 8d**) are enabled by this effective ICL with small *V*_{oc} loss and high FF (> 0.80).³² In addition, *V*_{oc} and FF of large-area devices are comparable to those seen in small-area devices, suggesting the promise of this ICL in scaling up all-PTSCs. Accordingly, a PCE of 21.4% has been achieved for 12 cm² device by adopting the

same ICL.⁴³ Notably, the efficiencies of 3J all-PTSCs also increase significantly due to robust ALD-SnO₂/Au-based ICL.^{21, 51} A record PCE of 20.1% with *V*_{oc} of 2.8 V and FF of 81.1% are obtained by ALD-SnO₂/Au-enabled efficient interconnection, with optimal bandgaps of 1.99, 1.60, and 1.22 eV for the front, central, and rear subcells, respectively (**Figure 8e**).²¹ A highly transparent, thick NiO layer is implemented in this work for interface engineering to yield a compact HTL (80 nm NiO/8 nm PTAA) for the subsequent central subcell fabrication (**Figure 8f**).²¹ In another study via assembling 1.73 eV wide-, 1.57 eV mid-, and 1.23 eV narrow-bandgap perovskite absorbers, a PCE of 16.8% for monolithic 3J all-PTSCs is attained with the ICL of C₆₀/SALD-SnO₂/Au/PEDOT:PSS, where SALD represents atmospheric pressure spatial-ALD.⁵¹ It is notable that as conventional ALD technique requires vacuum, it has a low deposition rate and thus is very time-consuming. By contrast, SALD operates at a much higher deposition rate and is closer to industrial requirement. The high deposition rate not only enables conformal and pinhole-free depositions, but also leads to the formation of large grains with fewer grain boundaries and thus improved transmittance and conductivity.³⁹

3.2.3 Highly Conductive PEDOT:PSS RL

Highly conductive poly(3,4-ethylenedioxythiophene)-poly(styrenesulfonate) (PEDOT:PSS) was exploited as a RL in the early stage of ICL study for all-PTSCs. PEDOT:PSS is a conductive organic semiconductor with high transparency from near UV to near IR region. Remarkably, the conductivity of PEDOT:PSS can be markedly improved by many orders of magnitude through post-treatment (i.e., secondary doping) with various compounds (e.g., salts, zwitterions, cosolvents, acids, alcohols, and phenols), making it comparable to ITO and suitable as a transparent electrode. Depending on different doping levels, PEDOT:PSS can operate as HTL or electrode. Highly conductive PEDOT:PSS with appealing transparency and ductility renders it a promising candidate as RL. Commercial PEDOT:PSS (PH1000) with a conductivity of 0.2-1 S/cm,⁵⁶ a widely used conductive electrode in optoelectronic devices, has been explored as RL for all-PTSCs.^{23, 41} Yet, these studies on PEDOT:PSS RL are not performed with optimized subcells (**Table 1**), resulting large V_{oc} loss and relatively low FF (**Figure 4**). In this context, the implementation of PEDOT:PSS RL with optimized subcells is the key to provide reliable evaluation and insight into its further improvement. In addition, the development of PEDOT:PSS as an efficient RL is rather restrained due to the following two issues. First, PEDOT:PSS is usually dispersed in H_2O . The direct spin-coating of PEDOT:PSS may damage the underneath perovskite subcell. Second, simple HTL/PEDOT:PSS/ETL may fail to function

as chemical barrier during the rear perovskite subcell fabrication. In this context, organic-solvent-soluble PEDOT:PSS with appropriate doping level and dense film-forming characteristic may render it more appealing RL for use in all-PTSCs. This can be a subject of future research.

Nonetheless, PEDOT:PSS was first introduced as a RL in a MAPbI₃-MAPbI₃ TSC.²³ The ICL is structured as spiro-OMeTAD/PEDOT:PSS/PEI/PCBM/PEI, during which a cationic polymer polyethylenimine (PEI) is used to modify the surface and form a work function contrast between the top and bottom sides of the PEDOT:PSS film via electrostatic interaction between positively charged PEI and negatively charged PEDOT:PSS. A film transfer lamination technique is used to form PEDOT:PSS RL from its aqueous solution. Notably, this ICL is robust to support the solution-processed perovskite top cell because of the incorporation PEI/PCBM/PEI ETL.²³ By contrast, a similar ICL with the structure of Spiro-OMeTAD/PEDOT:PSS/C₆₀ was found not compatible with solution processing of the subsequent perovskite film.⁴¹ Clearly, a material that promotes the interaction with the constituent layer in ICL would enable the formation of a dense ICL with efficient solvent resistance capability. By extension, the use of a crosslinking agent will also render a dense ICL to protect the bottom subcell against solvent penetration, thereby dispensing with the need for the deposition of thick TCO or SnO₂ layers as chemical barrier.

3.2.4 Ambipolar Material-based ICL

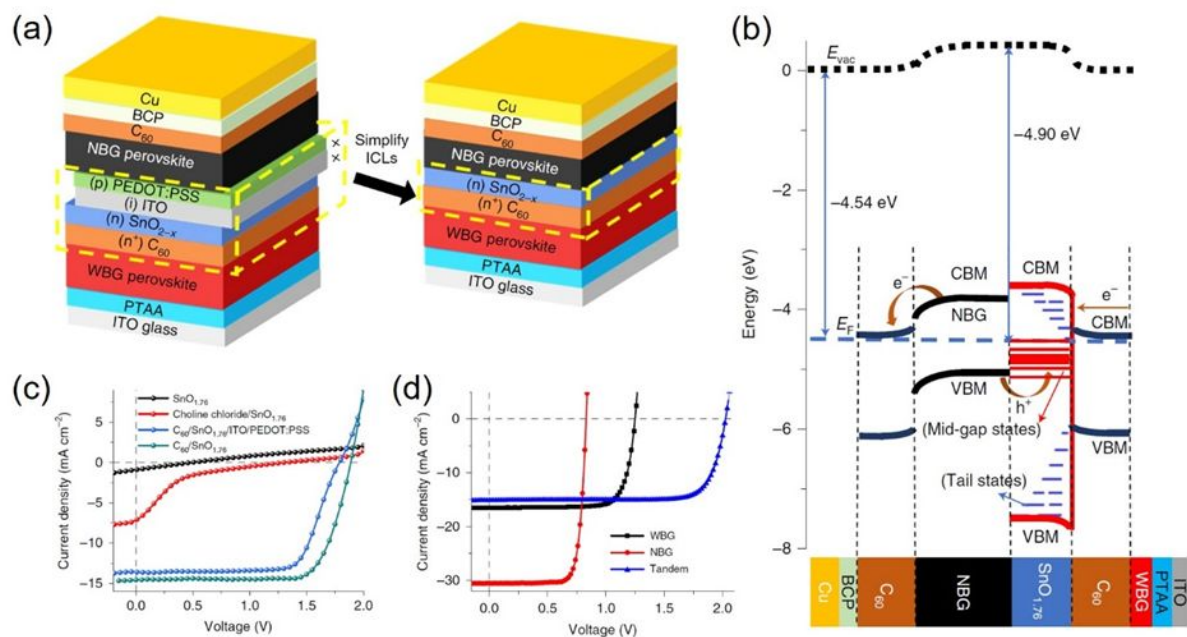


Figure 9. (a) Schematic diagram of tandem devices based on the ICL of C₆₀/SnO_{2-x}/ITO/PEDOT:PSS and simplified ICL of C₆₀/SnO_{2-x}. (b) Energy diagram of the C₆₀/SnO_{1.76} ICL-based all-PTSC. (c-d) J - V curves of all-PTSCs with (c) various ICLs and (d) C₆₀/SnO_{1.76} ICL. Reproduced with permission from Ref ³³. Copyright 2020, Springer Nature.

As noted in **Section 3.2.1-3.2.2**, ALD-SnO₂ has been broadly implemented as an outstanding chemical barrier in ICL for all-PTSCs while providing superior electron extraction as an ETL. Yet, recently, incomplete oxidization of tin was reported to form ALD-SnO_{2-x} (0 < x < 1), which demonstrates an ambipolar carrier transport property due to the co-existence of Sn²⁺ and Sn⁴⁺.³³ The incorporation of Sn²⁺ leads to a mid-gap band at ~0.8 eV, which enables the hole transport and forms ohmic contact with the rear perovskite subcell (**Figure 9b**). Such an ambipolar carrier mobility is truly revolutionary for constructing ICL in all-PTSCs, as it enables ALD-SnO_{2-x} to currently function as an ETL for the front subcell, an HTL for the rear subcell, and a RL for charge recombination, in addition to provide chemical barrier. The greatly simplified ICL consisting of C₆₀ (15 nm)/ SnO_{1.76} (9 nm) not only outperforms the typical ICL of C₆₀/SnO_{1.76}/ITO/PEDOT:PSS (**Figure 9a and 9c**) by avoiding the parasitic absorption from the ITO and PEDOT:PSS, but also improves the stability by eliminating the possible damage caused by the deposition of the ITO and PEDOT:PSS layers. As a result, PCEs of 24.4% (**Figure 9d**) and 22.2% are achieved with small-area (5.9 mm²) and large-area (1.15 cm²) devices, respectively. This seminal work on the n⁺/n (i.e., C₆₀/SnO_{1.76}) stack-based ICL demonstrates a new materials concept that ICLs for TSCs do not necessarily require both n-doped and p-doped layers to ensure decent electrical interconnections between subcells.

4. Path forward towards PCE >30%

Despite promising recent advances in RL-based ICL, considerable efforts are still required to increase PCE >30% and promoting large-area production of all-PTSCs. To this end, we outline the scientific and practical challenges in achieving robust ICLs and outlook concerning materials design and development, ICL characterization, ICL stability and scalability in order to realize full potential of ICL for high-efficiency and stable all-PTSCs.

4.1 Material design for ICL in all-PTSCs

4.1.1 Development of new ETL and HTL for ICL.

To render efficient TJ- and RL-based ICLs, carrier extraction layers are essential. In contrast to single-junction PSCs only requiring one transparent carrier extraction layer, all-PTSCs, by extension TSCs, necessitate the transparent ETL and HTL in ICL. Despite a large variety of organic and inorganic materials developed as effective ETL (TiO₂, SnO₂, C60, etc.) and HTL (spiro-OMeTAD, PEDOT:PSS, NiOx, etc.), only some of them are suitable to be applied in ICL considering the issues involving their fabrication compatibility with perovskites, optical transparency, and long-term stability. The widely-used HTL, spiro-OMeTAD, in single-junction PSC resulted in large parasitic absorption in blue and UV region when employed in ICL all n-i-p structured all-PTSCs.⁵⁷ Particularly, the acidic and hygroscopic PEDOT:PSS is the only most widely used HTL in ICL for all-PTSCs with a p-i-n configuration, yet found to be highly reactive with Pb-Sn narrow-bandgap perovskites.⁵⁸ Clearly, it is highly desirable to develop new transparent ETL and HTL with great chemical inertness with perovskites, for constructing efficient ICL with greatly enhanced

stability. This calls for substantial efforts not only from chemistry and materials science communities, but also theory community. Particularly, machine learning, as a powerful computational tool to formulate the structure–property relationship of new materials, is envisioned to greatly accelerate the development of robust carrier extraction layers.

Specifically, the complicated fabrication of ICL and parasitic absorption due to the thick ICL represent two significant limitations that may hinder the broad application and attainable PCE of TSCs, respectively. Recently, a simplified ICL based on ambipolar SnO_{1.76} was constructed for all-PTSCs.³³ In this context, the use of ambipolar two-dimensional semiconductors (e.g., graphene;⁵⁹ black phosphorene;⁶⁰ and metal chalcogenides (MoS₂, MoSe₂, WSe₂, etc.)⁶¹) with outstanding gate-controlled capability and unique physical properties could open up an avenue to craft ICL with new architectures (i.e., a greatly simplified ICL). Particularly, the development of organic ambipolar materials with the ability to crosslink may lead to breakthrough over current ICL of rather complex architectures, as they impart a multi-functional ICL, that is, simultaneously performing as ETL, HTL and solvent barrier

4.1.2 Towards enhanced charge recombination in ICL.

For TJ-based ICL, further degenerate doping is advantageous to decrease the width of the depletion region and thus enhance carrier recombination, as all-PTSCs capitalizing on simple organic ETL/HTL stacks as TJ-based ICL report low PCE due to significant losses associated with low Voc and FF.²² Since it is often difficult to concurrently achieve degenerate doping in both ETL and HTL in TJ-based ICL, particularly for those commonly used materials in single-junction PSCs, this entails the development of new ETL and HTL materials that can be conveniently doped. In this context, lessons may be learned from tandem organic light-emitting diodes and small molecule weight organic photovoltaics, as small-molecule organic semiconductors exploited in these devices demonstrate largely tunable conductivity over several orders of magnitude by simply varying the dopant concentration.⁶² Particularly, hydrophobic dopants are preferred to ensure the long-term stability all-PTSCs. In addition to degenerate doping, interfacial engineering represents a vital strategy to promote the quality of HTL/ETL stack for efficient charge recombination. To this end, placing self-assembled monolayers (SAMs) that conformally cover the ETL/HTL interface may stand out as a promising means of greatly improving the HTL/ETL stack interface.⁶³

For RL-based ICL, the ALD-SnO₂/Au combination exemplifies the most encouraging candidate, displaying negligible Voc loss and high FF (FF > 0.8 in 3J all-PTSCs).^{21, 32, 43, 51} Yet, it is appealing to replace expensive noble metal Au to earth-abundant Cu to reduce cost towards industrial application. It is notable that Ag is not appropriate as alternative replacement to Au as I⁻ ions migrating from the perovskite film could react with it. Other materials with suitable work function, widely used as transparent electrodes in optoelectronic devices, such as graphene and CNT, are also potential RL candidates.

4.1.3 Chemical protection over solution-processed all-PTSCs.

The ability of low-temperature solution processing affords all-PTSCs low-cost fabrication and compatibility with flexible substrates, yet requires a good interdiffusion barrier against solvent penetration, thereby protecting the subcell underneath. To date, this chemical barrier has been provided primarily by hard materials, such as sputtered ITO^{10, 27, 42} and ALD-SnO₂^{32, 43, 51} which, however, limits the extensive research on all-PTSCs due to accessibility to the needed instruments. Recently, PSCs with crosslinkable ETL and HTL have been reported with markedly improved photo, moisture, and thermal stability,⁴⁹ signifying their promising potential for affording chemical protection. Soft chemical barrier enabled by the crosslinked carrier extraction layers opens up an avenue towards all solution-processed ICL with excellent solvent resistance.²⁶ In the viewpoint of structures, crosslinking can be performed either by synthesizing new materials containing crosslinkable functional groups (e.g., alkyl side chains⁶⁴) or by incorporating crosslinkable small molecular agents in the host materials. The latter approach is relatively facile as it could readily employ commercially available agents, dispensing with the need for complex synthesis of the former. In addition, it is of particularly importance in performing crosslinking under mild conditions (e.g., low temperature, visible light etc.) due to the stability issues of underlying perovskite absorber. On the other hand, development of alternative solvents to DMF and DMSO for perovskite precursor dissolution can provide an additional strategy to avoid chemical damage of the bottom perovskite. For example, the use of highly-volatile acetonitrile(CH₃CN)/methylamine(CH₃NH₂) solvent mixture has been found to render solution processing of MAPbI₃ and MAPb_{0.75}Sn_{0.25}I₃.^{29, 65}

4.2 ICL Characterizations

Considering the complexity of the multilayer structure in ICL, its optimization can be extremely time-consuming, which thus highlights its comprehensive characterization prior to fabricating into tandem devices to avoid working laboriously on tandem prototypes. Investigations into the properties and performance of the ICL is a sophisticated process, which includes morphology, electrical, optical and mechanical characterization corresponding to its functions in TSCs. Overall, a standardized technique for this, as well as the definition of key diagnostic parameters, are yet to be established.⁵⁵ However, based on the routine characterization techniques and theoretical simulations, much information is attainable to accelerate the improvement of ICL for TSCs.

Since the topography is decisive for the deposition method or the resulted film quality and required thickness of the subsequent layers, gaining insights into the morphological properties of the underneath perovskite absorber and ICL allows better deposition of ICL and top perovskite absorber, respectively. The morphology characteristics of the ICL in terms of complete coverage, roughness, thickness, etc., can be carried out via scanning electron microscopy (SEM), scanning transmission electron microscope (STEM), and atomic force microscopy (AFM) studies. The complete surface coverage of ICL is essential in TSCs to avoid shunt and short paths. In addition to the influence on the top perovskite deposition, the surface topography of ICL also strongly affect light scattering and thus

reflection and interference in the layer stack.⁶⁶ Similarly, the layer thickness has a great effect on the optical properties of ICL as well, such as parasitic absorption. Notably, conformal and thin ICL can be fabricated via monitoring and improving the morphology of the underlayers to decrease the optical loss in the all-PTSCs. It has been reported ALD-AZO as a sputter buffer layer and an interdiffusion barrier in ICL, was significantly thinned by using an ultrathin PEIE (1 nm) as nucleation layer.³⁰

For the electric characterization, first the electronic properties of the different functional layers in ICL stack may be obtained using photoelectron spectroscopy, such as X-ray photoelectron spectroscopy (XPS) and ultraviolet photoelectron spectroscopy. Together with optical spectroscopy (e.g., UV-vis), band edge positions of the materials in ICL are available for understanding the charge transfer energetics. The carrier mobilities and charge carrier densities of the functional materials can be assessed using Hall measurements to gain insight of the carrier transport properties. Particularly, the electric resistivity or sheet resistance study of the RL in ICL is needed to identify a large lateral resistance and avoid shunts in large area devices.³⁰ As for the ICL performance, an immediate method to understand its electronic properties is to evaluate the diode's performance of the ICL junction.⁵⁵ This approach is commonly used among III-V multi-junction tandem research.^{55, 67, 68}

To characterize the optical properties of functional materials in the ICL, optical transmittance and reflectance spectra by spectrophotometry, as well as spectroscopic ellipsometry techniques are well-established techniques for daily experiments. In addition, the EQE and IQE measurements also provide the overall response of tandem devices. With these methods, parasitic absorption and back reflectivity of the layers in ICL can be analyzed. For TJ-based ICL, the optical characterization should be conducted with doped films as it has been reported that the parasitic absorption increases upon on doping in organic materials.^{69, 70} It is worth noting that for TCO RL-based ICL, an increased conductivity is usually accompanied by increased parasitic absorption in the IR part of optical spectrum.⁷¹ This tradeoff between high conductivity and sufficient optical transparency therefore highlights the importance of the optical and electric characterization.

Regarding the mechanical characterization, permeability tests of the ICL with polar solvents (i.e., DMF and DMSO) is first suggested as it would easily identify the ability of ICL against solvent penetration and facilitate thickness tuning of ICL. The measurement on Young's modulus, toughness, thermal expansion coefficient, as well as glass transition temperature of the functional layers in ICL can deliver important information that reflects the internal mechanical stresses in the ICL stack.⁷² Though such basic and easy characterization, the mechanical reliability of ICL used in all-PTSCs can be predicated.

In addition to experimental characterization, theoretical simulations, including optical simulation and electrical simulation, are powerful tools to gain detailed insights into the loss in all-PTSCs. It is worth noting that there is open access and commercial software available for both optical simulation and electrical simulation in any given specific solar cell architecture.⁶⁶

With optical simulation, it is easy to determine the impact of reflections and parasitic absorbance for any function layer in ICL with given thickness, and this has already been carried out in several reports.^{29, 44, 73} As for electrical simulation, detailed information related to the charge generation in perovskite absorber, charge transfer and recombination in ICL can be obtained to yield knowledge on performance-limiting factors such as barriers at heterojunctions and density of recombination centers at different locations in ICL.^{74, 75} In a next step toward improved ICL for all-PTSCs, simulations are expected to play a greater role in largely simplifying this process, thus avoiding intensive labor in experimental investigation on tandem prototypes.

4.3 ICL & Device stability

Though the instability of perovskite absorbers is the biggest challenge in all-PTSCs, device stability reflects the collective stability profiles of the wide-bandgap front subcell, narrow-bandgap rear subcell, ICL, and the interfaces. Thus, rational ICL design is an important part in improving the environment and operation stability of all-PTSCs. The primary principle of ICL design in terms of device stability can be addressed from two perspectives. First is the stability of ICL itself, that is, the functional materials incorporated in ICL including ETL, HTL and RL need to be stable, non-reactive with perovskite absorbers under various conditions and are better to be hydrophobic. Second is the role of the ICL in promoting the stability of the resulting all-PTSCs. This contains different aspects such as protecting the underneath subcell, benefiting the deposition of top subcell, and maintaining the long-term stability of all-PTSCs.

Among various functional layers in ICL, it is worth noting that HTL is the most unstable component for either n-i-p or p-i-n structured all-PTSCs. The thermal stability of the functional layers in ICL plays an important role as an annealing at ≥ 100 °C of the top subcell fabricated on ICL is usually needed. However, spiro-OMeTAD as the most commonly used HTL in ICL for n-i-p structured all-PTSCs,^{23, 29, 41} is especially unstable at elevated temperature. Besides, the hygroscopic dopants, usually lithium salt, used to increase the hole extraction and transfer ability of spiro-OMeTAD, would result in the poor operational stability of the devices. To improve ICL for n-i-p structured all-PTSCs, efforts on increasing glass transition temperature of spiro-OMeTAD, replacing hygroscopic dopants with hydrophobic ones, as well as developing alternative HTL are needed. Currently, high-performance all-PTSCs are all fabricated with a p-i-n structure as the mixed Pb–Sn subcell demonstrates higher PCE in p-i-n configuration.⁷⁶ This is because that the oxidation of Sn²⁺ into Sn⁴⁺ would form a layer of n-type SnOx on the top surface of Pb–Sn perovskite, which will block hole transfer to HTL in n-i-p structured device yet not block electron transfer to ETL in p-i-n structured device.^{29, 77} Notably, PEDOT:PSS is the only widely used HTL in ICL for p-i-n structured all-PTSCs. Yet, it is found to react adversely with Pb–Sn perovskites, which leads to severely worsened charge extraction and thermal stability.⁴⁰ This is currently one of the most urgent problems related to ICL improvement in all-PTSCs with a p-i-n configuration. Fortunately, the replacement of acidic PEDOT:PSS into neutral PEDOT:PSS has shown to largely extend the lifetime of mixed Pb–Sn PSCs,⁴⁰

which is expected to benefit the stability of all-PTSCs. For future study, strategies such as adding a buffer layer,³¹ adopting alternative HTL (e.g., NiOx),⁷⁸ and developing HTL-free rear subcell^{33, 79} deserve further exploration to avoid this reactivity issue between between PEDOT:PSS and Pb–Sn perovskite. Specifically, NiOx is most stable HTL reported to date. Yet, PSCs with NiOx HTL usually suffer from lower performance compared to PEDOT:PSS HTL-based devices.^{80, 81} Improvements on the preparation of NiOx HTL and the corresponding interfaces which enhance the performance of NiOx HTL-based single junction devices, are promising to promoting the implementation of NiOx in all-PTSCs.⁸²

As for the influence of the ICL on the stability of the all-PTSCs, it is mainly related to its deposition techniques and morphology, and the latter is dictated by the former. Considering the complexity of the multilayer structure in ICL, a combination of different deposition methods is usually adopted, including solution processing (e.g., spin-coating), evaporation, sputtering and atomic layer deposition (ALD). Spin-coating, as one of the most convenient and low-cost deposition method, has been widely used to prepare ETLs (e.g., PCBM), HTLs (e.g., spiro-OMeTAD, PEDOT:PSS, PTAA) and even RL (e.g., ITO nanoparticles, PEDOT:PSS)²⁹ in the ICL stack. Yet, solution processing is highly substrate dependent, and often leads to pinholes, cracks, and non-uniform coverage on rough substrates.^{83, 84} These defects, on one hand, can act as a point of ingress for solvent in processing the top sub-cell and cause detrimental effects to the bottom subcell; on the other hand, they would affect the uniform deposition and crystallization of the top perovskite, leading to more defects in the top perovskite absorber layer and may result in shunts or even short in the tandem cells. This would all decrease the stability of the resulting tandem devices. Notably, these issues mentioned above in solution processing can be minimized via modifying the solution and substrate characteristics. The addition of a self-assembled monolayer has been reported to enable the uniform and conformal coating of functional layers on the CIGS layer with a large surface roughness of 1 μm .^{63, 85} The use of multiple thin layers is also beneficial to minimize the influence of defects because it can disrupt the growth of defects and increase the solvent diffusion path length.⁸⁶ Similarly, more improvements are expected in the future study to further promote the application of low-cost solution processing of ICL and also deal with the solvent permeation. Compared to solution processing, evaporation, sputtering and ALD are much easier to achieve a conformal, uniform and pinhole free film on rough substrates. Additionally, the introduction of nucleation layers can further improve the growth of the subsequent layer via these techniques.³⁰ The application of these three methods in ICL deposition can be found in **Table 1**. Notably, the morphology and film quality of ICL stack also play a significant role in the long-term stability of all-PTSCs. A highly conformal ICL not only functions as a solvent barrier layer, but also acts as a good ion diffusion barrier to avoid ion penetrating from or into subcells, thereby enhancing the operation and long-term stability of tandem devices. Specifically, TCOs in ICL can effectively prevent ion diffusion and unfavorable reactions, thus play a positive role in enhancing device stability. On the contrary, the use of ultrathin metal as RL

in ICL may pose a problem as metal ingress from the top contact during device operation has been found to exacerbate perovskite degradation.^{80, 87} Yet, further experimental exploration is needed before excluding ultrathin metal from ICL due to the tiny amount used and other hard materials involved in ICL as a diffusion barrier.

It is worth noting that there are lots of internal and external mechanical stresses in solar cells, which can result in fracture and delamination in devices during operation. The internal stresses are usually generated due to thermal expansion coefficient difference between the layers, as well as thermal excursions and damage accumulation during operation while the external stresses can result from deformation (e.g., bending, stretching, and twisting) during manufacturing, installation, maintenance and service.^{72, 88, 89} Specifically, the thermal expansion coefficient difference induced internal stresses in all-PTSCs are predicted to be much higher than that in single junction PSCs due to the multi-layer structure, which thus largely enhances the risk of delamination. Though currently there are less reports dealing with the delamination in all-PTSCs, experience may be learnt from that in single junction PSCs. The approaches developed to enhance the toughness of the interface in single junction PSCs, such as adding interfacial layers, scaffolding, interpenetrating interfaces, as well as introducing additives, are also applicable in all-PTSCs.^{88, 90-92} Specifically, a self-assembled monolayer (SAM) has recently been developed to increase the adhesive toughness at the interface between ETL and perovskite to enhance the mechanical reliability of single junction PSC,⁷² thus highlights the application of SAM as multifunctional layers. Last but not the least, in addition to the strategies discussed above, the development of encapsulation plays a crucial role in protecting the device from external stimuli and enables decent long-term operational stability.

4.4 ICL up-scalability

Currently, nearly all the all-PTSCs are fabricated with small areas with several reports on 1 cm² devices.^{10, 20, 32, 33} This is mainly because that compared to single junction PSCs, the difficulty in fabricating tandem devices and scaling them up is much larger due to their complicated structure. Yet, the ability to scale up devices is a critical step towards future application and commercialization. Regarding the scale-up fabrication of the ICL for all-PTSCs, it can be discussed from two aspects, that is, material properties and deposition techniques.

As for the ICL properties, one important issue which is less studied in small area all-PTSCs is the lateral conductivity. As it has been known in the Si tandem community for years, the ICL in tandem devices should have good vertical conductivity to facilitate charge recombination through the junction yet minimal in-plane conductivity to minimize the spatial impact of shunts. The in-plane conductivity of ICL may exert a minimal effect in small area tandems, yet significantly affect the performance of large-area tandem devices or tandem solar modules. To date, the well-performed all-PTSCs have been all fabricated based on RL-based ICL (**Table 1**). Due to the conductive properties of RL, minimize the lateral conductivity of RL-based ICL is more critical and urgent in all-PTSCs scalability. As discussed in **Section 3.2**,

ITO and ultrathin Au are the two most widely used RL in the ICL for all-PTSCs. Though relatively small Voc loss and high FF are achieved with ITO RLs, its high lateral conductivity may limit its use in large-area all-PTSCs, especially for ITO RL with large thickness of ~100-120 nm. However, it has recently been demonstrated to reduce the lateral conductivity of TCO RL in all-PTSCs.³⁰ The fabrication of a thin and conformal PEIE(1 nm)/AZO(25 nm)/IZO(5 nm) RL resulted in a RL with sheet resistances on the order of 10⁻¹⁰⁰ K Ω /sq,³⁰ which is significantly higher than a 120 nm thick ITO recombination layer at ~30 Ω cm⁻².²⁷ This high sheet resistance can significantly inhibit lateral conduction to shunt pathways and is expected to pave the way of TCO RL for use in large-area all-PTSCs or solar modules. Regarding the ultrathin Au RL, a thickness of ~1 nm is usually adopted in practical application (**Table 1**). Though there is no report on measuring the sheet resistance of 1 nm Au RL-based ICL, a large sheet resistance is expected since the Au film should be discontinuous with such a thin thickness. Specifically, the recently developed ambipolar material SnO_{1.76} not only greatly simplifies the conventional RL-based ICL,³³ but also excludes the use of conductive materials as RL, thereby displaying promising application in all-PTSCs modules. While the TCO with large sheet resistance, ultrathin Au and ambipolar SnO_{1.76} function as promising candidates for use in RL-based ICL in large-area all-PTSCs, systematic studies and improvement on their lateral resistance are still needed in future study.

As showed in **Table 1**, solution processing (mostly spin-coating), evaporation, sputtering and atomic layer deposition (ALD) are widely used deposition techniques in ICL fabrication. While evaporation and sputtering are well-established industrial techniques, sputtering uses more energy and heat compared to evaporation. Thus, neutralization or other advanced approaches to manage the energetic plasma in sputtering should be used in the future study to minimize its damage to soft materials.⁷⁶ As for conventional ALD which requires vacuum, its low deposition rate and time-consuming characteristics limit its application in large-scale deposition. Fortunately, the atmospheric pressure spatial-ALD (SALD), working under atmospheric pressure at a much higher deposition rate in all-PTSCs, paves the way towards industrial operation.⁵¹ Notably, it has been reported that high deposition rate in ALD facilitates the formation large grains while retaining conformal and pinhole-free deposition, thus leading to improved transmittance and conductivity.³⁹ For solution processing, it is important to transfer from spin-coating to more scalable techniques, such as blade coating, slot-die coating, bar coating, spray coating, inkjet printing and screen printing.^{93, 94} It is worth noting that up-scaling a thin film technology is not trivial and often needs systematic modifications, which is of great importance since the morphology and film quality of the ICL would significantly affect both the bottom and top subcell, as well as the efficiency and stability of the tandem devices (**Section 4.3**). In the context, experience can be learned from the single junction PSCs to avoid working laboriously on tandem prototypes.

5. Conclusion

All-PTSCs exercise the same working mechanism as single-junction counterparts, yet containing an ICL as an additional key

constituent to concurrently provide electric, optical, and mechanical interconnections. In addition to the wide and narrow bandgap perovskite subcells, ICL is a critical part that dragging the development of all-PTSCs. Fortunately, continuous efforts have led to all-PTSCs with efficiency exceeding that of the best-performing single-junction PSCs recently. Yet, to further push the efficiency evolution of all-PTSCs, further understanding on ICL and its improvement represents an important endeavor. In this review, the essential characteristics of ICL in monolithic all-PTSCs is presented, aiming at providing guiding principles for new materials and engineering designs for ICL. Subsequently, recent progress in viable TJ-based ICL and RL-based ICL employed for all-PTSCs are discussed. Finally, we analyze the main scientific and practical challenges of ICL in terms of materials and structure design, characterization, stability and scalability. Identifying these challenges would enable the PSCs community to better address these issues with creative solutions, thus rendering all-PTSCs for industrial applications as affordable photovoltaic system.

Conflicts of interest

There are no conflicts of interest to declare.

Acknowledgements

The work is supported by the NSF (ECCS1914562) and AFOSR (FA9550-19-1-0317).

Notes and references

School of Materials Science and Engineering, Georgia Institute of Technology, Atlanta, GA 30332, USA. E-mail: zhiqun.lin@mse.gatech.edu

1. Y. Wang, Y. Zhang, P. Zhang and W. Zhang, *Phys. Chem. Chem. Phys.*, 2015, **17**, 11516-11520.
2. C. Wehrenfennig, G. E. Eperon, M. B. Johnston, H. J. Snaith and L. M. Herz, *Adv. Mater.*, 2014, **26**, 1584-1589.
3. S. D. Stranks, G. E. Eperon, G. Grancini, C. Menelaou, M. J. Alcocer, T. Leijtens, L. M. Herz, A. Petrozza and H. J. Snaith, *Science*, 2013, **342**, 341-344.
4. D. Shi, V. Adinolfi, R. Comin, M. Yuan, E. Alarousi, A. Buin, Y. Chen, S. Hoogland, A. Rothenberger and K. Katsiev, *Science*, 2015, **347**, 519-522.
5. N. R. E. Laboratory, Best Research-Cell Efficiency Chart (2021), <https://www.nrel.gov/pv/cell-efficiency.html>.
6. W. Shockley and H. J. Queisser, *J. Appl. Phys.*, 1961, **32**, 510-519.
7. C. H. Henry, *J. Appl. Phys.*, 1980, **51**, 4494-4500.
8. M. Anaya, G. Lozano, M. E. Calvo and H. Míguez, *Joule*, 2017, **1**, 769-793.
9. Z. J. Yu, M. Leilaoui and Z. Holman, *Nat. Energy*, 2016, **1**, 1-4.
10. G. E. Eperon, T. Leijtens, K. A. Bush, R. Prasanna, T. Green, J. T.-W. Wang, D. P. McMeekin, G. Volonakis, R. L. Milot and R. May, *Science*, 2016, **354**, 861-865.
11. T. Leijtens, K. A. Bush, R. Prasanna and M. D. McGehee, *Nat. Energy*, 2018, **3**, 828-838.
12. J. H. Noh, S. H. Im, J. H. Heo, T. N. Mandal and S. I. Seok, *Nano Lett.*, 2013, **13**, 1764-1769.
13. G. E. Eperon, S. D. Stranks, C. Menelaou, M. B. Johnston, L. M. Herz and H. J. Snaith, *Energy Environ. Sci.*, 2014, **7**, 982-988.
14. R. E. Beal, D. J. Slotcavage, T. Leijtens, A. R. Bowering, R. A. Belisle, W. H. Nguyen, G. F. Burkhard, E. T. Hoke and M. D. McGehee, *J. Phys. Chem. Lett.*, 2016, **7**, 746-751.
15. W. Ke, C. C. Stoumpos and M. G. Kanatzidis, *Adv. Mater.*, 2019, **31**, 1803230.
16. F. Hao, C. C. Stoumpos, R. P. Chang and M. G. Kanatzidis, *J. Am. Chem. Soc.*, 2014, **136**, 8094-8099.
17. J. Im, C. C. Stoumpos, H. Jin, A. J. Freeman and M. G. Kanatzidis, *J. Phys. Chem. Lett.*, 2015, **6**, 3503-3509.
18. H. Li and W. Zhang, *Chem. Rev.*, 2020, **120**, 9835-9950.
19. S. Gu, R. Lin, Q. Han, Y. Gao, H. Tan and J. Zhu, *Adv. Mater.*, 2020, **32**, 1907392.
20. R. Lin, J. Xu, M. Wei, Y. Wang, Z. Qin, Z. Liu, J. Wu, K. Xiao, B. Chen and S. M. Park, *Nature*, 2022, 1-9.
21. K. Xiao, J. Wen, Q. Han, R. Lin, Y. Gao, S. Gu, Y. Zang, Y. Nie, J. Zhu and J. Xu, *ACS Energy Lett.*, 2020, **5**, 2819-2826.
22. J. H. Heo and S. H. Im, *Adv. Mater.*, 2016, **28**, 5121-5125.
23. F. Jiang, T. Liu, B. Luo, J. Tong, F. Qin, S. Xiong, Z. Li and Y. Zhou, *J. Mater. Chem. A*, 2016, **4**, 1208-1213.
24. D. Forgács, L. Gil - Escrig, D. Pérez - Del - Rey, C. Mombiona, J. Werner, B. Niesen, C. Ballif, M. Sessolo and H. J. Bolink, *Adv. Energy Mater.*, 2017, **7**, 1602121.
25. A. Rajagopal, Z. Yang, S. B. Jo, I. L. Braly, P. W. Liang, H. W. Hillhouse and A. K. Y. Jen, *Adv. Mater.*, 2017, **29**, 1702140.
26. C.-Y. Chang, B.-C. Tsai, Y.-C. Hsiao, M.-Z. Lin and H.-F. Meng, *Nano Energy*, 2019, **55**, 354-367.
27. D. Zhao, C. Chen, C. Wang, M. M. Junda, Z. Song, C. R. Grice, Y. Yu, C. Li, B. Subedi and N. J. Podraza, *Nat. Energy*, 2018, **3**, 1093-1100.
28. C. Li, Z. S. Wang, H. L. Zhu, D. Zhang, J. Cheng, H. Lin, D. Ouyang and W. C. Choy, *Adv. Energy Mater.*, 2018, **8**, 1801954.
29. D. P. McMeekin, S. Mahesh, N. K. Noel, M. T. Klug, J. Lim, J. H. Warby, J. M. Ball, L. M. Herz, M. B. Johnston and H. J. Snaith, *Joule*, 2019, **3**, 387-401.
30. A. F. Palmstrom, G. E. Eperon, T. Leijtens, R. Prasanna, S. N. Habisreutinger, W. Nemeth, E. A. Gaubling, S. P. Dunfield, M. Reese and S. Nanayakkara, *Joule*, 2019, **3**, 2193-2204.
31. Z. Yang, Z. Yu, H. Wei, X. Xiao, Z. Ni, B. Chen, Y. Deng, S. N. Habisreutinger, X. Chen and K. Wang, *Nat. Commun.*, 2019, **10**, 1-9.
32. R. Lin, K. Xiao, Z. Qin, Q. Han, C. Zhang, M. Wei, M. I. Saidaminov, Y. Gao, J. Xu and M. Xiao, *Nat. Energy*, 2019, **4**, 864-873.
33. Z. Yu, Z. Yang, Z. Ni, Y. Shao, B. Chen, Y. Lin, H. Wei, J. Y. Zhengshan, Z. Holman and J. Huang, *Nat. Energy*, 2020, **5**, 657-665.
34. J. M. Ball, L. Buizza, H. C. Sansom, M. D. Farrar, M. T. Klug, J. Borchert, J. Patel, L. M. Herz, M. B. Johnston and H. J. Snaith, *ACS Energy Lett.*, 2019, **4**, 2748-2756.
35. J. F. Wheeldon, C. E. Valdivia, A. Walker, G. Kolhatkar, T. J. Hall, K. Hinzer, D. Masson, S. Fafard, A. Jaouad and A. Turala, 2009.
36. M. Yamaguchi, *Sol. Energy Mater. Sol. Cells*, 2003, **75**, 261-269.
37. T. Ameri, G. Dennler, C. Lungenschmied and C. J. Brabec, *Energy Environ. Sci.*, 2009, **2**, 347-363.
38. K. A. Bush, A. F. Palmstrom, J. Y. Zhengshan, M. Boccard, R. Cheacharoen, J. P. Mailoa, D. P. McMeekin, R. L. Hoye, C. D. Bailie and T. Leijtens, *Nat. Energy*, 2017, **2**, 1-7.
39. C. Li, Y. Wang and W. C. Choy, *Small Methods*, 2020, **4**, 2000093.
40. T. Leijtens, R. Prasanna, K. A. Bush, G. E. Eperon, J. A. Raiford, A. Gold-Parker, E. J. Wolf, S. A. Swifter, C. C. Boyd and H.-P. Wang, *Sustainable Energy & Fuels*, 2018, **2**, 2450-2459.
41. R. Sheng, M. T. Hörantner, Z. Wang, Y. Jiang, W. Zhang, A. Agosti, S. Huang, X. Hao, A. Ho-Baillie and M. Green, *J. Phys. Chem. C*, 2017, **121**, 27256-27262.
42. J. Tong, Z. Song, D. H. Kim, X. Chen, C. Chen, A. F. Palmstrom, P. F. Ndione, M. O. Reese, S. P. Dunfield and O. G. Reid, *Science*, 2019, **364**, 475-479.
43. K. Xiao, R. Lin, Q. Han, Y. Hou, Z. Qin, H. T. Nguyen, J. Wen, M. Wei, V. Yeddu and M. I. Saidaminov, *Nat. Energy*, 2020, **5**, 870-880.

44. K. Datta, J. Wang, D. Zhang, V. Zardetto, W. H. Remmerswaal, C. H. Weijtens, M. M. Wienk and R. A. Janssen, *Adv. Mater.*, 2021, 2110053.
45. J. H. Heo and S. H. Im, *physica status solidi (RRL)–Rapid Research Letters*, 2014, **8**, 816-821.
46. C. Momblona, L. Gil-Escrig, E. Bandiello, E. M. Hutter, M. Sessolo, K. Lederer, J. Blochwitz-Nimoth and H. J. Bolink, *Energy Environ. Sci.*, 2016, **9**, 3456-3463.
47. J. Ávila, C. Momblona, P. Boix, M. Sessolo, M. Anaya, G. Lozano, K. Vandewal, H. Míguez and H. J. Bolink, *Energy Environ. Sci.*, 2018, **11**, 3292-3297.
48. B. L. Watson, N. Rolston, K. A. Bush, L. Taleghani and R. H. Dauskardt, *J. Mater. Chem. A*, 2017, **5**, 19267-19279.
49. Z. Zhu, D. Zhao, C.-C. Chueh, X. Shi, Z. Li and A. K. Y. Jen, *Joule*, 2018, **2**, 168-183.
50. T. Leijtens, G. E. Eperon, N. K. Noel, S. N. Habisreutinger, A. Petrozza and H. J. Snaith, *Adv. Energy Mater.*, 2015, **5**, 1500963.
51. J. Wang, V. Zardetto, K. Datta, D. Zhang, M. M. Wienk and R. A. Janssen, *Nat. Commun.*, 2020, **11**, 1-10.
52. P. Liu, X. Liu, L. Lyu, H. Xie, H. Zhang, D. Niu, H. Huang, C. Bi, Z. Xiao and J. Huang, *Appl. Phys. Lett.*, 2015, **106**, 193903.
53. F. Sahli, B. A. Kamino, J. Werner, M. Bräuninger, B. Paviet - Salomon, L. Barraud, R. Monnard, J. P. Seif, A. Tomasi and Q. Jeangros, *Adv. Energy Mater.*, 2018, **8**, 1701609.
54. K. Brinkmann, T. Becker, F. Zimmermann, C. Kreuzel, T. Gahlmann, M. Theisen, T. Haeger, S. Olthof, C. Tüchtmantel and M. Günster, *Nature*, 2022, **604**, 280-286.
55. M. De Bastiani, A. S. Subbiah, E. Aydin, F. H. Isikgor, T. G. Allen and S. De Wolf, *Materials Horizons*, 2020, **7**, 2791-2809.
56. H. Shi, C. Liu, Q. Jiang and J. Xu, *Advanced Electronic Materials*, 2015, **1**, 1500017.
57. Š. Daškevičiūtė, N. Sakai, M. Franckevičius, M. Daškevičienė, A. Magomedov, V. Jankauskas, H. J. Snaith and V. Getautis, *Adv. Sci.*, 2018, **5**, 1700811.
58. X. Zheng, A. Y. Alsalloum, Y. Hou, E. H. Sargent and O. M. Bakr, *Accounts of Materials Research*, 2020, **1**, 63-76.
59. K. S. Novoselov, A. K. Geim, S. V. Morozov, D. Jiang, Y. Zhang, S. V. Dubonos, I. V. Grigorieva and A. A. Firsov, *science*, 2004, **306**, 666-669.
60. M. Zhang, M. Ye, W. Wang, C. Ma, S. Wang, Q. Liu, T. Lian, J. Huang and Z. Lin, *Adv. Mater.*, 2020, 2000999.
61. W. Hu, Z. Sheng, X. Hou, H. Chen, Z. Zhang, D. W. Zhang and P. Zhou, *Small Methods*, 2021, **5**, 2000837.
62. K. Walzer, B. Maennig, M. Pfeiffer and K. Leo, *Chem. Rev.*, 2007, **107**, 1233-1271.
63. A. Al-Ashouri, A. Magomedov, M. Roß, M. Jošt, M. Talaikis, G. Chistiakova, T. Bertram, J. A. Márquez, E. Köhnen and E. Kasparavičius, *Energy Environ. Sci.*, 2019, **12**, 3356-3369.
64. R.-Q. Peng, P.-J. Chia, J.-C. Tang, B. Liu, S. Sivaramakrishnan, M. Zhou, S.-H. Khong, H. S. Chan, J. H. Burroughes and L.-L. Chua, *Nat. Mater.*, 2010, **9**, 152-158.
65. N. K. Noel, S. N. Habisreutinger, B. Wenger, M. T. Klug, M. T. Hörantner, M. B. Johnston, R. J. Nicholas, D. T. Moore and H. J. Snaith, *Energy Environ. Sci.*, 2017, **10**, 145-152.
66. M. Jošt, L. Kegelmann, L. Korte and S. Albrecht, *Adv. Energy Mater.*, 2020, **10**, 1904102.
67. W. Guter and A. W. Bett, *IEEE Transactions on Electron Devices*, 2006, **53**, 2216-2222.
68. V. Andreev, E. Ionova, V. Larionov, V. Rumyantsev, M. Shvarts and G. Glenn, 2006.
69. X. Fan, W. Nie, H. Tsai, N. Wang, H. Huang, Y. Cheng, R. Wen, L. Ma, F. Yan and Y. Xia, *Adv. Sci.*, 2019, **6**, 1900813.
70. W. H. Nguyen, C. D. Bailie, E. L. Unger and M. D. McGehee, *J. Am. Chem. Soc.*, 2014, **136**, 10996-11001.
71. M. Morales - Masis, S. De Wolf, R. Woods - Robinson, J. W. Ager and C. Ballif, *Advanced Electronic Materials*, 2017, **3**, 1600529.
72. Z. Dai, S. K. Yadavalli, M. Chen, A. Abbaspourtamijani, Y. Qi and N. P. Padture, *Science*, 2021, **372**, 618-622.
73. K. Jäger, L. Korte, B. Rech and S. Albrecht, *Optics express*, 2017, **25**, A473-A482.
74. A. Singh and A. Gagliardi, *Solar Energy*, 2019, **187**, 39-46.
75. N. Singh, A. Agarwal and M. Agarwal, *Solar Energy*, 2020, **208**, 399-410.
76. T. Moot, J. Werner, G. E. Eperon, K. Zhu, J. J. Berry, M. D. McGehee and J. M. Luther, *Adv. Mater.*, 2020, **32**, 2003312.
77. M. Konstantakou and T. Stergiopoulos, *J. Mater. Chem. A*, 2017, **5**, 11518-11549.
78. Q. Han, Y. Wei, R. Lin, Z. Fang, K. Xiao, X. Luo, S. Gu, J. Zhu, L. Ding and H. Tan, *Sci Bull*, 2019, **64**, 1399.
79. R. Prasanna, T. Leijtens, S. P. Dunfield, J. A. Raiford, E. J. Wolf, S. A. Swifter, J. Werner, G. E. Eperon, C. de Paula and A. F. Palmstrom, *Nat. Energy*, 2019, **4**, 939-947.
80. C. C. Boyd, R. Cheacharoen, K. A. Bush, R. Prasanna, T. Leijtens and M. D. McGehee, *ACS Energy Lett.*, 2018, **3**, 1772-1778.
81. K. A. Bush, A. F. Palmstrom, Z. J. Yu, M. Boccard, R. Cheacharoen, J. P. Mailoa, D. P. McMeekin, R. L. Hoye, C. D. Bailie and T. Leijtens, *Nat. Energy*, 2017, **2**, 1-7.
82. W. Chen, Y. Zhou, G. Chen, Y. Wu, B. Tu, F. Z. Liu, L. Huang, A. M. C. Ng, A. B. Djurišić and Z. He, *Adv. Energy Mater.*, 2019, **9**, 1803872.
83. F. Sahli, J. Werner, B. A. Kamino, M. Bräuninger, R. Monnard, B. Paviet-Salomon, L. Barraud, L. Ding, J. J. Diaz Leon and D. Sacchetto, *Nat. Mater.*, 2018, **17**, 820-826.
84. M. Liu, M. B. Johnston and H. J. Snaith, *Nature*, 2013, **501**, 395-398.
85. A. Magomedov, A. Al - Ashouri, E. Kasparavičius, S. Strazdaite, G. Niaura, M. Jošt, T. Malinauskas, S. Albrecht and V. Getautis, *Adv. Energy Mater.*, 2018, **8**, 1801892.
86. G. L. Graff, R. E. Williford and P. E. Burrows, *J. Appl. Phys.*, 2004, **96**, 1840-1849.
87. K. Domanski, J.-P. Correa-Baena, N. Mine, M. K. Nazeeruddin, A. Abate, M. Saliba, W. Tress, A. Hagfeldt and M. Grätzel, *ACS nano*, 2016, **10**, 6306-6314.
88. Q. Dong, C. Zhu, M. Chen, C. Jiang, J. Guo, Y. Feng, Z. Dai, S. K. Yadavalli, M. Hu and X. Cao, *Nat. Commun.*, 2021, **12**, 1-9.
89. S. K. Yadavalli, Z. Dai, H. Zhou, Y. Zhou and N. P. Padture, *Acta Materialia*, 2020, **187**, 112-121.
90. N. Rolston, A. D. Printz, J. M. Tracy, H. C. Weerasinghe, D. Vak, L. J. Haur, A. Priyadarshi, N. Mathews, D. J. Slotcavage and M. D. McGehee, *Adv. Energy Mater.*, 2018, **8**, 1702116.
91. B. L. Watson, N. Rolston, A. D. Printz and R. H. Dauskardt, *Energy Environ. Sci.*, 2017, **10**, 2500-2508.
92. J. Tong, J. Gong, M. Hu, S. K. Yadavalli, Z. Dai, F. Zhang, C. Xiao, J. Hao, M. Yang and M. A. Anderson, *Matter*, 2021, **4**, 1365-1376.
93. Z. Li, T. R. Klein, D. H. Kim, M. Yang, J. J. Berry, M. F. Van Hest and K. Zhu, *Nat. Rev. Mater.*, 2018, **3**, 1-20.
94. D. Li, D. Zhang, K. S. Lim, Y. Hu, Y. Rong, A. Mei, N. G. Park and H. Han, *Adv. Funct. Mater.*, 2021, **31**, 2008621.

Cite this: DOI: 10.1039/c1ee00000x

www.rsc.org/ees

REVIEW
